

FRIEDRICH-ALEXANDER-UNIVERSITÄT ERLANGEN-NÜRNBERG
LEHRSTUHL FÜR STRÖMUNGSMECHANIK

CHALMERS UNIVERSITY OF TECHNOLOGY, GÖTEBORG
DEPARTMENT OF THERMO AND FLUID DYNAMICS

Master Thesis

Multi-Point Similarity of the
Axisymmetric Turbulent Far Jet
and Its Implication for the POD

Bettina Frohnapfel

August 2003

Supervisors:

Prof. Dr. Dr. h.c. F. Durst

Prof. Dr. W. K. George

Assoc. Prof. Dr. T. G. Johansson

Asst. Prof. Dr. P. Johansson

Abstract

The Proper Orthogonal Decomposition (POD) is an experimental and theoretical tool used to investigate coherent structures in a turbulent flow. The goal is to decompose the actual random field (e.g. the velocity field) into orthogonal functions that can be treated mathematically. The resulting integral equation can be solved if the flow is either homogeneous or of finite extent. None of these solutions work in the streamwise direction of an axisymmetric jet, since the flow is neither homogeneous nor bounded in this direction.

A few years ago it was shown theoretically that similarity solutions of the two-point Reynolds stress equations were possible, so that the POD could be applied in similarity coordinates and the complexity of the streamwise direction of the jet could be treated by transforming it to a homogeneous field in the similarity variables. In this work this theory is tested using two-point cross-correlation measurements with separations in the streamwise directions. The experimental demands associated with such measurements are very high because of the need to obtain the streamwise velocity correlations. This means that the measuring device located at the upstream point must not disturb the measurements at the downstream position. This hurdle has been overcome by using a combination of a laser Doppler anemometer (LDA) measuring the upstream point and a constant temperature anemometer sensor (CTA) measuring the downstream position.

An experiment has been designed and set up that allows the investigation of the far turbulent axisymmetric jet. The jet properties were determined and the jet was shown to truly behave as a free jet in the investigated region. For the correlation measurements, the two measuring techniques were successfully combined and two-point correlations in the streamwise direction (along the centerline) were obtained that indeed show homogeneous behavior in similarity variables as proposed by theory. Furthermore, strong indications were found that it is possible to apply Taylor's Frozen Field Hypothesis to this highly turbulent flow.

Finally, the same ideas are shown to apply to recent PIV data.

Acknowledgements

This thesis was written as a cooperative project of LSTM, Erlangen and the Chalmers University of Technology in Gothenburg, Sweden.

First of all I would like to thank Prof. F. Durst of the LSTM Erlangen for setting up the contact with Prof. W.K. George at Chalmers. Without his support this thesis would not have been possible. A big thank you goes also to Prof. George who invited me to join his turbulence research group. I had a great time here at Chalmers and definitely learned a lot, be it in front of one of the many helpful chalkboards or scribbled on a napkin while having a cup of cappuccino.

Setting up the experiment and sorting out the problems that arose would not have been possible without the help of Dr. T. Gunnar Johansson and Dr. Peter B.V. Johansson. Thanks so much for your support and for always being there when I had questions. Thanks also to Lars Jernquist for the help with the electronics.

Prof. Emig, head of the chair of Technical Chemistry II in Erlangen, showed great interest in the interdisciplinary topic of this thesis and thus in cooperation with Prof. Durst made it possible to catch the interest of GlaxoSmithKline. Thanks to him and to GSK, particularly Dr. Christian Auriou, for the interest in this research. The provided financial support is greatly acknowledged.

I would also like to thank Dr. J. Jovanovic and Dr. S. Becker of the LSTM in Erlangen for the revision of the script.

Finally, I would like to thank everyone at Chalmers for their very warm welcomes and for providing a great working and free time atmosphere. Special thanks to Elteyeb, Lucas, Vinay, Mattias and Benjamin, who worked with me as part of their Experimental Course back in February. The set-up of the experiment, especially of our big tent, became significantly easier and faster with that many hands to help.

Contents

List of Figures	vii
Index of symbols	viii
1 Introduction	1
2 The Axisymmetric Turbulent Jet	4
2.1 Introduction	4
2.2 Similarity Analysis of the Jet	7
2.2.1 Single Point Statistics	7
2.2.2 Multi-Point Statistics	9
3 Proper Orthogonal Decomposition (POD)	11
3.1 Introduction	11
3.2 An Overview of the POD Theory	12
3.3 The Far Jet	13
4 Experimental Techniques	14
4.1 Hot-Wire Anemometry	15
4.2 Laser Doppler Anemometry	18
4.2.1 Fundamentals	18
4.2.2 Residence Time Weighting	23
4.2.3 Particle Size	24
4.3 Combination of the Techniques	25
4.3.1 Simultaneous Operation of the Devices	25
4.3.2 Acquisition of Simultaneous Data	26
5 The Experiment	30
5.1 Experimental Set Up	30
5.2 The Enclosure	31
5.3 Properties of the Jet	34
5.4 Spatial Correlation Measurements	38

6	Measurement Accuracy	40
6.1	Preliminary Measurements	40
6.2	Operating Conditions	42
6.2.1	Measuring Time	42
6.2.2	Hot Wire Settings	43
6.2.3	Seeding	43
6.3	Spatial Correlation	43
6.4	Effect of Hot-Wire Errors	45
7	Results	47
7.1	Two-Point Correlations	47
7.2	Scaled Two-Point Correlations	48
7.3	Taylor's Frozen Field Hypothesis	49
7.4	Implication of Taylor's Hypothesis and Similarity for Spectra	52
7.5	Measured Spectra	53
8	PIV Results and Future Work	58
9	Summary	62
	Bibliography	64

List of Figures

2.1	The axisymmetric jet	5
4.1	Scheme of Constant Temperature Anemometer (CTA)	16
4.2	Calibration set-up	17
4.3	Doppler effect	19
4.4	Doppler effect with two illuminating waves	20
4.5	Intersection of two laser beams a) correct, b)incorrect	21
4.6	Doppler burst before and after passing the filter	22
4.7	Power Spectrum at $x/D=30.3$	25
4.8	Effect of smoke on hot wire	26
4.9	Calibration curves of the hot-wire before and after the use of smoke	27
4.10	CTA and LDA measurement in the same position	28
4.11	Simultaneous HW and LDA sampling	29
5.1	Measurement jet	31
5.2	Picture of the experimental set up	32
5.3	Velocity profiles at different downstream positions	34
5.4	Normalized velocity profiles	35
5.5	Turbulence intensity plotted against normalized radial position	35
5.6	Determination of the virtual origin x_o and the decay constant B	37
5.7	Determination of the virtual origin x_o and the growth rate of the jet	37
5.8	Set-up during a measurement	39
5.9	Schematic set-up of hot wire and LDA during a measurement	39
6.1	HW and LDA measurements at the same positions	41
6.2	Comparison with the curve fits obtained by Hussein <i>et al.</i> [31]	41
6.3	Autocorrelation at $x/D = 53.3$	42
6.4	Comparison between measurement on external and internal clock (corrected for time shift)	44

7.1	Two-point correlations at different downstream positions . . .	48
7.2	Two-point correlations in similarity variables	49
7.3	Spatial correlations in comparison with transformed autocorrelations	51
7.4	Spatial correlations and transformed autocorrelations in similarity variables	51
7.5	Power spectrum $S_{11}(f)$ at $x/D=30.3$ versus frequency f . . .	54
7.6	Power spectrum $S_{11}(f)$ at $x/D=43.3$ versus frequency f . . .	55
7.7	Power spectrum $S_{11}(f)$ at $x/D=58.3$ versus frequency f . . .	55
7.8	Comparison of the three power spectra. Note spectra at low frequencies are the same within uncertainty, consistent with similarity theory and applicability of Taylor's hypothesis . . .	56
7.9	Wavenumber spectra $F_{11}^1(k_1)$ at $x/D=30.3, 43.3$ and 58.3 versus wavenumber k_1	57
7.10	Scaled wavenumber spectra $\tilde{F}_{11}^1(\tilde{k}_1)$ at $x/D=30.3, 43.3$ and 58.3 versus scaled wavenumber \tilde{k}_1	57
8.1	Spatial correlation of the axial velocity fluctuations obtained from PIV data	59
8.2	Spatial correlation of the axial velocity fluctuations in similarity coordinates	60
8.3	Spatial correlation of the radial velocity fluctuations obtained from PIV data	60
8.4	Spatial correlation of the radial velocity fluctuations in similarity coordinates	61

Index of Symbols

Latin symbols

Symbol	Specification
A	constant
A_R	cross section of the enclosing roon
A_0	cross section of nozzle
B	decay constant
B_{11}	autocorrelation
B_u	constant, $B_u = \frac{1}{2}\pi^{\frac{1}{2}}B$
C	spatial correlation
C_{11}	spatial correlation of axial velocity fluctuations
C_{22}	spatial correlation of radial velocity fluctuations
$C_{0,1,2,3,4}$	constants
C_{u,v^2}	correlation coefficient
d_{beam}	diameter of unfocused laser beam
d_w	diameter of hot wire
d_1, d_2	major and minor axis of the ellipsoidal measuring control volume
D	nozzle diameter
\vec{e}_D	unit vector of the detection direction
\vec{e}_L	unit vector of the illuminating wave direction
f	frequency
f_l	focal length of the transmitting lens
f_N	wire cut-off point
$f(\eta)$	profile function
Δf	frequency band
F_{11}^1	wavenumber spectrum
\tilde{F}_{11}^1	scaled wavenumber spectrum
$g_{12}(\eta)$	profile function
h	heat transfer coefficient

Symbol	Specification
I	electric current
I_t	integral time scale
k_0	thermal conductivity
k_1	wavenumber
\tilde{k}_1	scaled wavenumber
K_u, K_v, K_w	normal stresses
l	constant length scale
l_w	length of hot wire
L_{11}	spatial integral scale
M	momentum of the flow
M_0	initial momentum of the flow
N	total number (of particles, independent samples, etc.)
Nu	Nusselt number
P	pressure
$Q_{i,j}$	2-point correlation in similarity variables
r	radial direction
$R, R_{i,j}, \overline{R_{i,j}}$	double point velocity correlation
R_s	shear stress
R_w	wire resistance
R_0	wire resistance at ambient temperature
Re	Reynolds number
$S_{11}(f)$	frequency spectrum
t	time
Δt	residence time
T	total record time
T_w	wire temperature
T_0	ambient temperature
Tu	turbulence intensity
u	fluctuating velocity component in axial direction
u^*	complex conjugate
u_m	measured velocity fluctuation
u_{rms}	rms value of axial velocity
\vec{u}	velocity of the flow
u_{\perp}	flow velocity perpendicular to the optical axis
\overline{uv}	Reynolds stress
U	instantaneous velocity
U_f	instantaneous fluid velocity
U_p	instantaneous particle velocity
U_c	centerline velocity

Symbol	Specification
U_{con}	convection velocity
\tilde{U}_m	instantaneous measured velocity
U_{mean}, \bar{U}	mean velocity
U_S	velocity scaling
U_R	velocity of return flow
U_0	outlet velocity
v	fluctuating velocity component in radial direction
v_{rms}	rms value of radial velocity
V	relative velocity between particle and fluid
x	downstream position
x^*	HW measurement position for transformed autocorrelation
$x * l$	$x * l = x^* + \Delta x^*$
x_0	virtual origin
Δx^*	$\Delta x^* = \tau * U_C$, virtual distance
Δx	fringe spacing

Greek symbols

Symbol	Specification
α	thermal resistance coefficient
δ	width of the jet
δ_s	length scaling
$\delta_{\frac{1}{2}}$	half width of the jet
ϵ	relative error
η	transformed coordinate in radial direction
φ	half the intersection angle of laser beams
ρ	scaled autocorrelation
ρ_f	fluid density
ρ_p	particle density
Φ_i	orthonormal coordinate system
λ	eigenvalue
λ_{laser}	wave length of the laser
μ	dynamic viscosity
ν	kinematic viscosity
ν_b	Bragg cell frequency
ν_{L1}, ν_{L2}	frequencies of intersecting laser beams
ν_s	frequency of laser after passing the Bragg cell
ν, ν', ν''	frequency
$\Delta\nu$	Doppler frequency
$\Delta\nu_s$	frequency of the movement of interference fringes
Θ	azimuthal direction
τ	time lag
ξ	transformed coordinate in axial direction
ψ	virtual location of transformed autocorrelation in similarity coordinates

Abbreviations

Abbreviation	Specification
BSA	Burst Spectrum Analyser
CCA	Constant Current Anemometry
CTA	Constant Temperature Anemometry
DNS	Direct Numerical Simulation
FFH	Taylor 's frozen field hypothesis
LDA	Laser Doppler Anemometry
LES	Large Eddy Simulation
HW	hot-wire
HWA	Hot-Wire Anemometry
PIV	Paritcle Image Velocimetry
POD	Proper Orthogonal Decomposition
rms	root mean square

Chapter 1

Introduction

The understanding of turbulent flows remains one of last mysteries of classical physics. Turbulence is a phenomenon that not only occurs in engineering applications, but also can be observed in most flows in nature. Over the past decades extensive theoretical and experimental work has been carried out trying to explain the underlying physics.

All fluid motions, turbulent flows as well as laminar flows, are governed by the Navier-Stokes equations, a set of differential equations. The problem is that due to the complex structures of turbulent flows these equations can even numerically only be solved for very small Reynolds numbers and simple geometries. The final goal is not only to solve those equations but also to find means by which it would be possible to control the turbulent flow. Thus it is essential to find simplifications to those equations.

In 1894 Osborne Reynolds [39] introduced the idea of decomposing the velocity into time mean and fluctuating components. Many investigations have been based on these so-called Reynolds-averaged Navier-Stokes equations, and different turbulence models found a starting point in them.

A different approach is to look at the turbulence structure in a flow and try to understand how it originated. One key feature of a turbulent flow is that it is not completely random but that there exist vortical structures. Thus turbulence is commonly viewed as a flow field consisting of eddies of different sizes. Those coherent structures appear to determine the macro characteristics of the flow, such as mass, momentum and energy transport. Understanding how these characteristics are related to structure would shed further insight into how to control and predict turbulence.

One of the great difficulties in the analysis of turbulent flows has been the absence of ways to break these scales or eddies of turbulence down into functions that can be treated mathematically. One method referred to as Proper Orthogonal Decomposition (POD) has become available only re-

cently due to the rapid development of computers. In this technique the actual velocity field is decomposed, starting with the most energetic modes, in a manner such that the original flow field can be recovered. The integral equation at the core of the POD can easily be solved for flows that are homogeneous or of finite extent. If neither is the case, a proper solution is not at hand.

Due to its simple geometry and wide application range, the free axisymmetric jet has been the base for many turbulence investigations. Its streamwise direction, in which the flow is neither homogeneous nor bounded, presents one of above mentioned cases where the POD cannot be applied properly. A few years ago it was shown theoretically by Ewing [15, 17] that equilibrium two-point similarity could be used to overcome the difficulties in the streamwise direction. The theory suggests rescaling the longitudinal direction so that the flow field in streamwise direction of the jet is transformed to a homogeneous field in the similarity variables.

Up to now the theory could not be verified due to a lack of suitable experimental data. The objective of this thesis is to obtain the streamwise velocity correlations to reveal whether in fact they can be rescaled to yield homogeneous behavior.

The required spatial correlation measurements are challenging. Traditionally, such measurements have been made using Constant Temperature Anemometry (CTA). This technique cannot be applied in the longitudinal direction because the wire downstream would be affected by the wake from the wire situated further upstream. The combination of two Laser Doppler Anemometers (LDA) has been reported for longitudinal correlation measurements in the boundary layer (Jordan and Gervais [32]) and the near field of the jet (Eriksson and Karlsson [14]).

For the required measurements in the far field of the jet it was decided not to use two LDA systems because of the comparatively low data rate to which this technique is limited. Instead, a combination of CTA and LDA was chosen. This combination could yield the desired data rate but also introduced additional problems that needed to be solved before the methodology could be applied. These were mainly related to the use of the hot wire in combination with the seeding particles required for the LDA and the simultaneous sampling with the two devices. In this experiment the two techniques were combined successfully, yielding results that support the theory. It was shown that the spatial correlations, obtained in the streamwise inhomogeneous direction of a turbulent free jet, can indeed be rescaled in a way that they indicate a homogeneous flow field in similarity variables.

At the beginning of this thesis single point and multi point statistics as well as the POD theory are briefly reviewed. The measurement techniques

are explained and it is described how their combination was accomplished. Finally the correlation measurements are presented and their behavior in similarity coordinates is discussed.

In addition to the spatial correlations, Taylor's Frozen Field Hypothesis was applied to the temporal autocorrelation curves obtained at the reference points for the spatial correlations. Surprisingly it seems to be possible to apply this theory to this highly turbulent flow at all scales of motion. This approach is extended and confirmed by analysis of the power and wavenumber spectra.

Chapter 2

The Axisymmetric Turbulent Jet

2.1 Introduction

Over the past years the axisymmetric turbulent jet has been studied extensively. This is due to the fact that on the one hand jets are easily generated and can be found in many engineering applications. On the other hand the jet is one of the simplest turbulent flows (next to the wake) which can be studied. Since the environment is at rest and there are no external boundaries, boundary conditions are homogeneous. The jets symmetry, although it only exists statistically, also reduces the complexity of the problem. Unfortunately, the high local turbulence intensities make experimental studies complicated.

A jet facility is usually designed so that the jet emerges from the source with a top-hat profile. In reality there will be found some overshoot depending on the design of the nozzle. Due to the high velocity difference between the core of the jet and the non-turbulent irrotational surrounding air, an axisymmetric mixing layer forms that grows as the flow evolves. The development of an axisymmetric jet is schematically shown in fig. 2.1. After a relatively short transition region, which depends on the Reynolds number of the jet, the mixing layer becomes fully turbulent. The continuously growing mixing layer in a low Mach number jet reduces the potential core at the center of the jet until it has completely vanished by about $x/D = 3$, and the velocity profile over the cross section does not show a flat region any longer. The evolution of the flow in this region is highly dependent on the initial conditions, especially on the Mach number.

The region up to $x/D = 5$ (at low Mach numbers) is considered to be

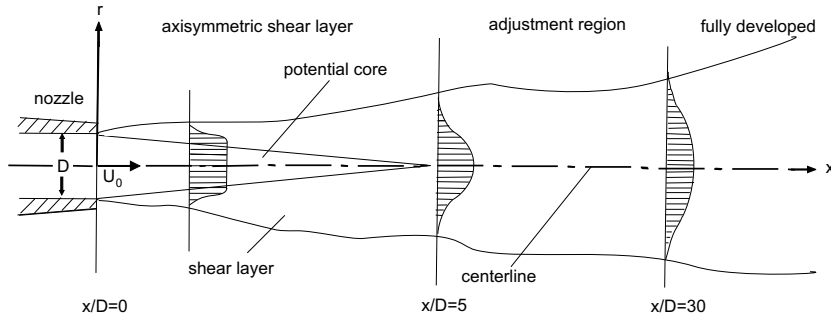


Figure 2.1: The axisymmetric jet

the near field of the jet or the axisymmetric shear layer. Subsequently the adjustment region is found. From approximately 30 diameters downstream the jet is fully developed and the velocity profile is similar when scaled in local variables, usually centerline velocity and halfwidth of the jet. Similarity analysis is concerned with this so-called far field of the flow.

One of the earliest investigations of the jet was first undertaken by Tollmien [43] in the 1920s. Through the past decades this flow has remained a matter of particular interest. (For an extensive review see Jung [33] and Gamard [19].) It is widely acknowledged that the dissipation of the turbulent kinetic energy occurs in the small scales of the flow. The large scales, that dominate the physics of the axisymmetric jet, can easily be made visible at low Reynolds numbers. Nevertheless, they remain largely a mystery, especially concerning the way energy is generated from the mean flow and how it is transferred to smaller scales (Hussain [30]).

Most studies of the large-scale structure focused on the potential core region, in part for its interest for noise-production but also because of the possibility to use flow visualisation techniques in this region. The Proper Orthogonal Decomposition (POD), first introduced to the turbulence community by Lumley in 1967 [36], is a powerful tool for the investigation of energetic structures. It was initially applied to jets by Arndt *et al.* [3, 4] and Glauser [25, 26].

The large quantity of data required to apply the POD to the velocity field limited the work of experimentalists until two-point measurements of adequate accuracy became available. Citriniti and George [12] were the first to apply the POD to a full cross-section of the flow using an array of 138 hot-wire probes. Jung [33, 34] continued their work using the same 138-wire probe. He investigated the large-scale structure of the axisymmetric mixing layer using the POD for different Reynolds numbers at $2 \leq x/D \leq 6$,

and showed that the energy distribution of the first POD modes had a strong dependence on x/D but had no Reynolds number dependency, at least above $Re=30,000$. This is consistent with suggestions by Glauser [27] and Citriniti and George [12] that there should not be a dependence once the Reynolds number is sufficiently high. With the advances in computers, many new investigations are being reported. A detailed review of the POD application to the near field of the axisymmetric jet can be found in Glauser *et al.* [27] and in Gamard [19].

The far field region of the jet is better known analytically due to the simplifications of a properly done similarity analysis as presented by George [23]. The high turbulence intensity in this region of the jet makes measurements rather difficult, and what is known about the evolution of large scale structures is derived mostly from flow visualization and conditional sampling studies. Wygnansky and Fielder [44] reported the first hot-wire measurements up to 90 diameters downstream. They however underestimated the problem of enclosure of the jet, a problem that was first recognized by Baker [5, 6] and investigated in detail by Capp [10] who applied burst-mode LDA techniques to measure jet profiles in different enclosures. The findings of Capp were confirmed by studies of Panchapakesan and Lumley [38] and Hussein, Capp and George [31]. Together, they provide a broad investigation of the single-point statistics in the far field region of the axisymmetric jet.

Gamard [19] applied a slice POD to the Far Region of an axisymmetric jet at distances from 20 to 69 diameters downstream. Using the experimental apparatus of Citriniti and George [12] and Jung [33] he showed that the normalized eigenspectra do not depend on the downstream distance in the equilibrium similarity region. Scaled in similarity variables, the eigenspectra were shown to collapse as proposed by the equilibrium similarity analysis of the two-point Reynolds stress equations by Ewing and George [17].

More generally this similarity analysis proposed that the flow field of a turbulent jet could be transformed into a homogeneous field in similarity variables for the streamwise and azimuthal direction. If this is true it will be possible to apply the POD in the streamwise direction, which cannot be done properly up to today due to its unbounded extent. In order to test this theory, two-point correlation measurements with separations in the streamwise direction of the far jet are required. Measurements of that kind did not exist prior to this investigation.

Traditionally, spatial correlation measurements were performed using hot-wire anemometry techniques. This is not possible for measurements of the longitudinal correlation, since the upstream wire will create a wake and disturb the signal at the second wire. Two-point correlation measurements using

the non-intrusive LDA technique have been reported (Jordan [32], Eriksson [14]). In those measurements small scales and the resolution required to obtain information about the dissipation of energy were of major interest. Even measurements using two LDAs are not easy, due to the difficulties of obtaining simultaneous realizations. This work used a combined LDA/hot-wire technique to exploit the advantages of each.

2.2 Similarity Analysis of the Jet

2.2.1 Single Point Statistics

The equations of the far field region of the ideal jet are known to admit to equilibrium similarity solutions. The possibility of those solutions was recognized by Tollmien [43] and others. Similarity analysis seeks solutions to the averaged equations of the form

$$U = U_s(x) f(\eta) \quad (2.1)$$

$$-\overline{uv} = R_s(x) g_{12}(\eta) \quad (2.2)$$

where

$$\eta = \frac{r}{\delta(x)}. \quad (2.3)$$

The similarity scales, U_s , R_s and δ , must be chosen so that the averaged equations become invariant with downstream position. Traditionally the scales are chosen such that the statistical moments are rescaled using a single length and velocity scale (Tennekes and Lumley [41]) so that

$$R_s = U_s^2. \quad (2.4)$$

This assumption can only be made if the growth rate $d\delta/dx$ of the jet is constant. It is also usually assumed that the scaled profiles are independent of the initial conditions of the flow, a condition that can be justified theoretically only if the source is presumed to be nothing but a point source of momentum [23, 37]. Further, in the traditional approach, it is argued that the asymptotic similarity solution for each type of flow is universal, that means that all jets should approach the same self-preserving state. This approach indeed

collapses the mean velocity profiles for all measured jets. Unfortunately the other moments and spreading rates appear to be source dependent [8].

A second approach, equilibrium similarity as suggested by George [23], is a more general analysis where arbitrary scales for all of the statistical moments in the transport equations are used to carry out the similarity analysis. The scales are determined by the transport equations themselves using the equilibrium similarity constraint that all relevant terms must maintain the same relative value downstream at a given value of the dimensionless radial coordinate. In this approach, a possible dependence on the initial and upstream conditions (denoted by the argument $*$) cannot be ruled out. Thus, the similarity solutions sought, must be of the form

$$U = U_s(x, *) f(\eta, *), \quad (2.5)$$

$$-\overline{uv} = R_s(x, *) g_{12}(\eta, *). \quad (2.6)$$

Using equilibrium similarity it is never assumed that $R_s = U_s^2$ as in the traditional approach but the shear stress R_s is found to have the following dependency

$$R_s \propto U_s^2 \frac{d\delta}{dx}. \quad (2.7)$$

Note that even when $d\delta/dx$ is a constant, as in the case considered here for the far jet, the constant of proportionality depends on initial (or upstream) conditions in general. Furthermore, it is shown that the normal stresses can be described by

$$K_u = K_v = K_w = U_s^2. \quad (2.8)$$

This relationship is of special interest for the presented work, since it makes it possible to scale the obtained correlation with the square of the rms-values instead of the centerline velocity.

The solutions derived from the traditional approach can be obtained using the second approach, the latter being more general since the scales for the velocity moments are not necessarily powers of the scale used for the mean velocity. The more general analysis also indicates that the attained self-preserving state could be uniquely determined by the initial conditions. Thus, in principle, virtually every jet could be unique. For the jet the consequences of self-preservation on higher order moments restore the linear growth rate, even though it need not be the same for all jets. Indeed

numerous recent experiments suggest strongly it is not [8, 19]. Also it turns out (theoretically) that the properly scaled mean velocity and Reynolds stress profiles are independent of the initial conditions, even though $d\delta/dx$ and the other moments are not. These more general single point equilibrium similarity solutions have been shown by many to describe real jets beyond $x/D \approx 30$ if they are not affected by confinement [31, 38].

Thus, equilibrium similarity theory, like the classical one, implies that it is justified to choose $U_s = U_c$ and $\delta_s = \delta_{\frac{1}{2}}$. Furthermore, it is shown that the decay of the centerline velocity U_c can be described by

$$\frac{U_0}{U_c} = B \left(\frac{x - x_0}{D} \right) \quad (2.9)$$

where U_0 is the exit velocity, B the decay constant, x_0 the virtual origin and D the outlet diameter of the jet. The growth rate of the jet is given by

$$\delta = A(x - x_0), \quad (2.10)$$

a linear dependency. Both factors of proportionality, A and B , reflect the initial conditions and are interrelated by the need to conserve overall momentum. For example, for the jet used in the experiment the constants were found to be $A = 2$ and $B = 6.5$; whereas for the low Reynolds number jet of the PIV measurement in Chapter 8 they are given by $A = 0.1$ and $B = 5.9$.

2.2.2 Multi-Point Statistics

Ewing and George [15, 16, 17] extended the equilibrium similarity analysis of the far axisymmetric jet to the two-point Reynolds stress equations that govern the evolution of the two-point velocity correlation tensor. They were able to show that the double point, single time, velocity correlation equations admit to equilibrium similarity solutions.

In brief, the length scale growth as the jet develops downstream is removed by defining a new coordinate system. Since the analysis of the single point moments shows that the Reynolds number based on similarity variables is constant for the axisymmetric jet ($\delta \propto x, U_c \propto 1/x$), it can be deduced that all physical length scales grow proportionally as the flow evolves and can therefore be scaled by one length scale.

In the radial direction the new coordinate system is equivalent to the one used in one point similarity, the transformed coordinate being

$$\eta = \frac{r}{\delta}. \quad (2.11)$$

Ewing further deduced that the transformed coordinate in the mean flow direction was

$$\xi = \ln \left(\frac{x - x_0}{l} \right) \quad (2.12)$$

where x_0 is the location of the virtual origin of the jet and l a constant length scale included for dimensional reasons. This transformation converts the streamwise coordinate in the axisymmetric jet from a semi-infinite coordinate x to a coordinate ξ that is infinite in extent. Interestingly, this result is obvious in hindsight, since in the far jet changes with x are proportional to x . Due to the symmetry of the jet, the azimuthal direction is of no further interest, at least for this work.

In general the double point velocity correlation tensor

$$R_{i,j} = \langle u_i(\cdot) u_j(\cdot') \rangle \quad (2.13)$$

has a dependency on all positions in regular variables.

$$R_{i,j} = R_{i,j}(x, x', r, r', \Theta, \Theta') \quad (2.14)$$

Ewing was able to show that it reduces to a dependency on the logarithmic difference in position, if scaled in the new variables.

$$R_{i,j} = U_s(x) U_s(x') \sqrt{\frac{d\delta}{dx} \frac{d\delta'}{dx'}} Q_{i,j}(\xi' - \xi, \eta', \eta, \Theta' - \Theta) \quad (2.15)$$

This implies that the appropriately scaled turbulence moments of the flow field of the far axisymmetric jet are homogeneous in the variables $\xi' - \xi$ and homogeneous periodic in $\Theta' - \Theta$. Gamard [19] was able to confirm part of this idea for a fixed downstream position; i.e., $\xi' - \xi = 0$, by correlating velocities acquired from a rake of 138 hot wires. It has never been possible to test the most interesting part of this prediction, namely the logarithmic streamwise dependence on $\xi' - \xi$.

The aim of this work was to test the validity of the theory for different streamwise separations for the same radial position. Two-point correlations were measured along the centerline $\eta = \eta' = 0$ starting at different downstream positions. If the governing equations for the velocity correlation at two arbitrary points in space indeed admit to similarity solutions, then the correlation curves obtained should collapse if plotted against $\xi' - \xi$, the similarity variable. Such collapse of the scaled streamwise correlations would suggest strongly that the theory is correct and applicable to real jets. The implications for the POD could be profound. This is not only interesting because of POD questions, but also because it could provide a vehicle for DNS and LES computations at much higher Reynolds numbers using existing computers.

Chapter 3

Proper Orthogonal Decomposition (POD)

3.1 Introduction

A theoretical approach to investigate coherent structures was introduced by Lumley (1967) [36] and is called Proper Orthogonal Decomposition (POD). The mathematics and underlying physics of its application have been discussed by numerous authors, among them Holmes, Lumley and Berkooz [29] and George [22, 24].

The mathematical basis is a Karhunen-Loève expansion. The goal is to decompose the actual velocity (or pressure) field into the most energetic modes, and in a manner so that the results can be used with the Navier-Stokes equations for further analysis and computation. The POD has only recently become heavily utilized because of the large amount of data required. With the advances in computer technology and the availability of reasonably accurate two-point measurements, the POD became a useful tool that has been applied to the jet experimentally and theoretically (see Gamard [19] for a review).

The POD results form a projection of the velocity field into a coordinate system that is optimal in terms of energy. The resulting integral equation can be solved if the flow is either homogeneous or of finite extent. But none of those solutions work in the streamwise direction of an axisymmetric jet, since the flow is neither homogeneous nor bounded in this direction. The result of a POD in this direction will always depend on the chosen domain.

If the proposed coordinate transformation that is tested in this thesis is correct, the streamwise direction of the jet reduces to a homogeneous field in the similarity variables. Then the POD could be applied in similarity

coordinates exactly like any other homogeneous field. Moreover the solutions are known to be analytical Fourier modes. Thus not only clues to POD become applicable, but its solution is known.

3.2 An Overview of the POD Theory

Mathematically, the core of the POD is a projection of a random velocity field $u_i(x, t)$ into an orthonormal coordinate system Φ_i optimal in terms of energy content; i.e. Φ needs to be defined so that

$$\frac{\langle (u_i, \Phi_i)^2 \rangle}{\|\Phi_i\|} = \lambda \quad (3.1)$$

is maximized. Using calculus of variations this can be shown to result into

$$\int_{region} R_{ij}(\cdot, \cdot') \Phi_j(\cdot') d(\cdot') = \lambda \Phi_i(\cdot) \quad (3.2)$$

where the kernel of this integral equation

$$R_{i,j} = \langle u_i(\cdot) u_j(\cdot') \rangle \quad (3.3)$$

is the two-point velocity correlation tensor and (\cdot) represents the spatial coordinates and time.

Depending on the integration field the solutions to this eigenvalue problem differ. If the field has finite total energy, like the radial direction of the jet, the Hilbert-Schmitt theory applies and the solution to equation 3.2 results directly from it. It is this particular application which is usually referred to as POD, since the eigenfunctions are orthogonal and the eigenvalues ordered ($\lambda_1 > \lambda_2 > \lambda_3$ etc.). Almost always the solutions are implemented numerically and the kernel is determined experimentally.

In the case of periodic, stationary or homogeneous dimensions (as in the azimuthal direction of the jet or in time) Fourier modes can be shown to be the appropriate choice for the eigenfunctions. In this case the eigenfunctions are known analytically, and the eigenvalues become eigenspectra (one for each Fourier mode). This behaviour is of special interest here. For example, consider only a scalar field and suppose the turbulence were homogeneous in x . Then the kernel would depend only on $x' - x$, instead of x' and x separately; i.e. $R(x', x) = \overline{R}(x' - x)$. Then equation 3.2 reduces to

$$\int_{region} \overline{R}(x' - x) \Phi(x') dx' = \lambda \Phi(x). \quad (3.4)$$

Using $z = x' - x$ this can be transformed to obtain

$$\int_{region} \overline{R}(z) \Phi(x+z) dz = \lambda \Phi(x). \quad (3.5)$$

Dividing both sides by $\Phi(x)$ yields

$$\int_{region} \overline{R}(z) \left[\frac{\Phi(x+z)}{\Phi(x)} \right] dz = \lambda. \quad (3.6)$$

The right side is independent of z (which is integrated over) and x . Therefore, Φ must be a function for which the term in brackets is independent of x . Only functions of exponential type satisfy this and only those with an imaginary argument do not decay or blow up. Therefore, $\Phi \propto e^{ikx}$ and the solutions are Fourier modes. Also λ is a function of k . In fact $\lambda(k)$ is the spectrum; or in this context, the eigenspectrum. Clearly homogeneity has powerful implications.

3.3 The Far Jet

None of these approaches apply to inhomogeneous flows of infinite extent, as is the case in the downstream direction of an axisymmetric jet. Recently Ewing [15] showed that it was possible to find similarity solutions of the two-point Reynolds stress equations for which the two-point correlation was homogeneous in the transformed variable $\xi = \ln(x/l)$. Ewing then showed that the POD could be applied in these similarity coordinates exactly as in the homogeneous case above where the eigenfunctions were harmonic functions in ξ . Thus homogeneity in ξ has a very important implication: it means that an intractable problem will not only have been made tractable, but the solution is known. If substantiated by experiment, the analytical eigenfunctions open many possibilities for further analysis of the instantaneous equations. One need only look at how Fourier modes are used in stability theory or DNS to understand the possibilities.

Chapter 4

Experimental Techniques

Earlier investigations of turbulent structures in the jet used Hot Wire Anemometry (HWA) as measuring technique (Gamard [20]). It is widely used for turbulence investigations since it is easy to use and a very sensitive device to measure velocity fluctuations. Nevertheless, in the jet with turbulence intensities above 25%, the HWA is operated on its limits and might yield falsified results (Hussein *et al.* [31]).

In order to take measurements at two different locations on the centerline of the jet simultaneously, it is not possible to use HWA in the upstream position since the wire would create a wake and disturb the flow downstream. It was therefore decided to use the non-intrusive Laser Doppler Anemometry (LDA) in the upstream position. This measuring technique requires seeding particles that have to be small enough to follow the flow so that particle and fluid velocity are identical. In order to receive unbiased data, uniform spatial distribution of those particles has to be ensured.

In the downstream position it was decided to use HWA. The use of two LDAs for the measurement of two-point correlations in a jet has been reported (Eriksson and Karlsson [14], Jordan and Gervais [32]). The problem with those measurements is the fact that a LDA does not provide a continuous signal like a HW, but there is only a signal available when a seeding particle crosses the measuring control volume. Due to the extremely low probability of two particles crossing the two different measuring volumes at exactly the same time it was decided not to use another LDA system in the downstream position.

The combination of LDA and HWA for correlation measurements in a jet has to the authors knowledge not been reported before. There are two major challenges inhibitant in that combination. First, it has to be ensured that the seeding particles required for the LDA do not affect the hot-wire and falsen its signal. Secondly, the time trace of the two measurements must be

available to identify the two signals, that were received at exactly the same time.

Correlation measurements in a jet are in principle also possible using Particle Image Velocimetry (PIV). With this measuring technique the entire flow field is captured at a single time. Its limitations however can be found in the comparatively small number of statistically independent samples that can be obtained, since the total amount of data acquired with this technique becomes too big to be handled conveniently.

4.1 Hot-Wire Anemometry

Hot-Wire Anemometry (HWA) is based on the physical phenomena of the linear dependence of a wire's resistance on its temperature. It measures the heat transfer from a thin heated wire to the surrounding moving fluid. There are two different modes of operation for a hot wire: constant current (CCA) and constant temperature anemometry (CTA). The latter one is the accepted standard.

The heat transfer from the wire depends on

- the relative velocity between the wire and the flow
- the temperature difference between the wire and the fluid
- the physical properties of the fluid
- the dimensions and physical properties of the wire
- external factors like e.g. proximity to a wall

In many applications the temperature of the fluid, its physical properties and the pressure are constant. With CTA the temperature difference between the wire and the fluid, the so-called overheat, is kept constant as well, so that the heat transfer becomes a function of the flow velocity only. In these experiments the overheat ratio was maintained at about 0.72 which is equivalent to a wire temperature 200°C above the ambient temperature.

The heat transfer from the wire has to be balanced by the heat generated by the current running through the wire,

$$I^2 R_w = h \pi d_w l_w (T_w - T_o) = \pi l_w k_0 (T_w - T_o) Nu \quad (4.1)$$

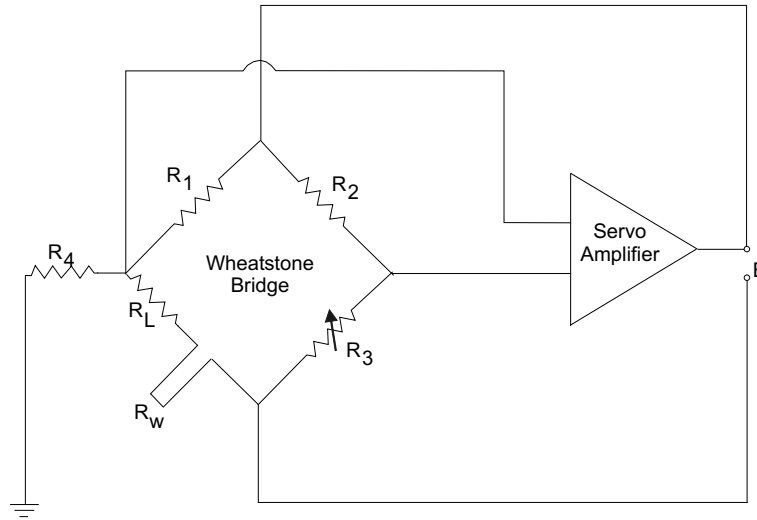


Figure 4.1: Scheme of Constant Temperature Anemometer (CTA)

where the indices w and o describe the wire and surrounding conditions respectively, h is the heat transfer coefficient, k_o the heat conductivity of air at the surrounding temperature and d_w and l_w are the dimensions of the wire.

Using the linear dependence of the wire resistance on the temperature

$$R_w = R_o [1 + \alpha (T_w - T_o)] \quad (4.2)$$

equation 4.1 can be rewritten as

$$\frac{I^2 R_w}{R_w - R_o} = \pi l_w k_o \frac{Nu}{\alpha R_o}. \quad (4.3)$$

The Nusselt number $Nu = hd_w/k_o$ represents the ratio between total and conductive heat transfer. The wires temperature changes are due to changes in forced convection, free convection, heat conduction and radiation, where the first one clearly dominates the process. In general, $Nu = Nu(Re)$ or alternatively $Re = Re(Nu)$, if all other dimensionless ratios are held constant. The former form is more common (e.g. King's Law), but the latter is generally more accurate and certainly easier to use (Beuther *et al.* [7]). In these experiments the Re number was expressed as a polynomial of Nu , or simply

$$U = C_0 + C_1 E + C_2 E^2 + C_3 E^3 + C_4 E^4 \quad (4.4)$$

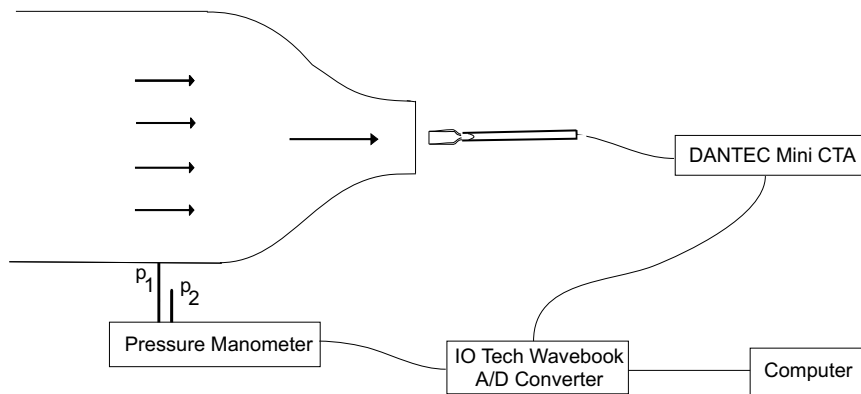


Figure 4.2: Calibration set-up

since all thermal properties were constant.

Modern commercial anemometers use a Wheatstone Bridge and a large feed back amplifier to keep the wire resistance constant. A scheme of a Wheatstone bridge used in Constant Temperature Anemometers is shown in fig. 4.1. A cooling of the wire results in a decrease of the wire's resistance. The drop of resistance in the wire creates a voltage difference between the two arms of the bridge. This difference is registered by the servo amplifier which in turn feeds the bridge with an additional current so that the wire element is heated until its resistance does not create a voltage difference any more. In case of a temperature increase of the wire the bridge is fed with a lower current allowing the wire temperature to drop to its initial value. The thermal time constant of the wire and the gain of the anemometer determine the frequency response of the wire/CTA system. In the present experiment this cutoff was at least an order of magnitude higher than that due to the spatial filtering of the wire itself. Typically, spatial filtering shows up at a convected frequency of approximately $f_N \approx U_c/2l_w$. For this experiment with a centerline velocity of $U_c=8$ m/s at 33 diameters downstream the wire cut-off point is found at $f_N < 2700$ Hz; on the other hand the temporal frequency response of the system is approximately 50 kHz.

Before and after being used, a hot wire has to be calibrated. Therefore, the wire is placed in a laminar flow of known velocity. A scheme of the calibration procedure is shown in fig. 4.2. The probe is positioned at the exit of a nozzle and a pressure tube is connected before the contraction. The pressure readings can be transformed into the outlet velocity using the continuity equation and the Bernoulli equation. The voltage differences

between the two arms of the Wheatstone bridge can thus be related to a known velocity as described by equation 4.4.

4.2 Laser Doppler Anemometry

4.2.1 Fundamentals

Laser-Doppler-Anemometry (LDA) is an optical non-intrusive method to measure the flow properties of gases, liquids and solids. The only necessary conditions are a transparent medium and a suitable concentration of tracer particles. A detailed description can be found in Durst *et al.* [13].

Doppler effect

Laser-Doppler-Anemometry is based on the Doppler shift of the light scattered from a moving particle. If transmitter and receiver are in relative motion, the sending frequency is different from the detected one. Light (laser beam) with a frequency ν is sent to a particle which moves with the velocity of the flow. Due to its motion it "sees" a different frequency ν'

$$\nu' = \frac{c - \vec{u} \cdot \vec{e}_L}{c} \nu \quad (4.5)$$

The incoming light is scattered towards the receiver, introducing an additional Doppler shift since the particle now acts as a moving transmitter (fig. 4.3)

$$\nu'' = \frac{c}{c - \vec{u} \cdot \vec{e}_D} \nu' \quad (4.6)$$

where \vec{u} is the velocity of the particle, c the speed of light and \vec{e} the unit vectors in the direction of the laser beam (L) and the detector (D).

The resulting Doppler shift is given by

$$\Delta\nu = \nu'' - \nu = \nu \left(\frac{c - \vec{u} \cdot \vec{e}_L}{c - \vec{u} \cdot \vec{e}_D} - 1 \right). \quad (4.7)$$

Simplification with series expansion ($|\vec{u}| \ll c$) yields

$$\Delta\nu = \vec{u} \frac{\nu}{c} \cdot (\vec{e}_D - \vec{e}_L) \quad (4.8)$$

The problem is that for the flow velocities of interest this frequency differs only slightly from the frequency of the illuminating wave. It is difficult to

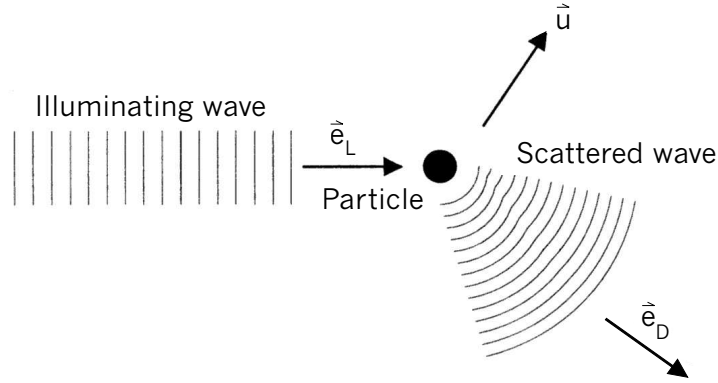


Figure 4.3: Doppler effect

resolve this difference. Therefore, in practice the light scattered from two intersecting laser beams is mixed. Usually, the laser beam is divided into two beams of identical intensity. In the ideal case the beams intersect in their respective beam waists, creating a measuring control volume (see fig. 4.5) whose size, based on the e^{-2} intensity cut-off point, is determined by

$$d_2 = \frac{4\lambda_{laser} f_l}{\pi d_{beam} \cos(\varphi)} \quad (4.9)$$

$$d_1 = \frac{4\lambda_{laser} f_l}{\pi d_{beam} \sin(\varphi)} \quad (4.10)$$

where λ_{laser} the laser wavelength, f_l the focal length of the transmitting lens, d_{beam} the diameter of the unfocused laser beam exiting from the focusing lens, and φ half the intersection angle of the beams.

A particle crossing the volume of intersection "sees" both beams (fig. 4.4). They are scattered towards the receiving optics with slightly different frequency shifts due to their different incoming angles. These two waves are super-imposed intermittently, interfering constructively and destructively. The result is the Doppler frequency ν_D (4.11), that can easily be resolved.

$$\nu_D = \nu_1'' - \nu_2'' = \vec{u} \frac{\nu}{c} (\vec{e}_{L,1} - \vec{e}_{L,2}) \quad (4.11)$$

Trigonometrical considerations yield

$$\nu_D = \frac{2 \sin \varphi}{\lambda} u_{\perp} \quad (4.12)$$

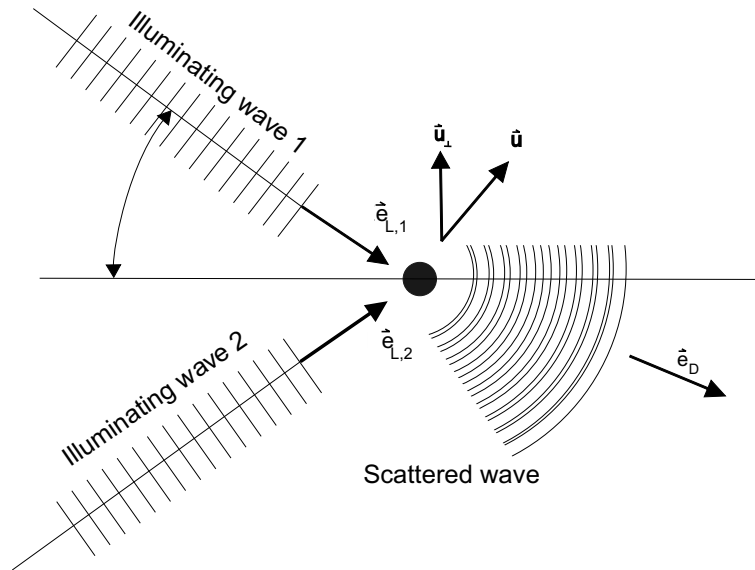


Figure 4.4: Doppler effect with two illuminating waves

where φ is half the angle between the incoming laser beams, λ the wave length of the laser light, and u_{\perp} the component of the fluid velocity in the direction perpendicular to the symmetry axis of the optics. The Doppler frequency is not dependent on the location of the receiver and furthermore directly proportional to the measured velocity component. Since the factor of proportionality consists of known quantities which remain unchanged during the measurement, LDA has an absolute linear response to fluid velocity and can be performed without calibration.

Model of interference fringes

The model of interference fringes can be used alternatively to explain the operation of the dual beam anemometer. It is not entirely correct but yields correct results in many regards and simplifies the description of LDA.

Laser Doppler Anemometry makes use of the wave character of light as well as of the coherence of laser light. The intersection of two laser beams produces an intersection volume with parallel planes of light and darkness as shown in fig. 4.5(a). These so-called fringes are caused by the interference of two laser beams in their waists.

The distance between the fringes Δx is a function of the wave length

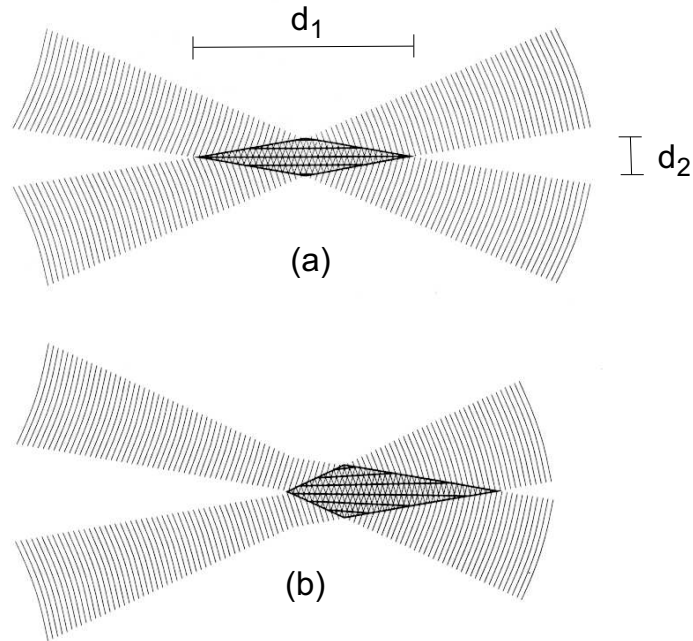


Figure 4.5: Intersection of two laser beams a) correct, b)incorrect

λ_{laser} of the laser light and the geometrical set up,

$$\Delta x = \frac{\lambda_{laser}}{2 \sin \varphi} \quad (4.13)$$

where φ is half the angle of intersection. Particles passing the measuring volume scatter the incoming light and therefore visualize the maxima and minima of intensity. From trigonometrical considerations it can be shown that

$$\nu_D = \frac{2 \sin \varphi}{\lambda} u_{\perp} \quad (4.14)$$

which is the same expression as obtained earlier based on the Doppler shift of the scattered light (equation 4.12). The frequency ν_D detected by the receiver indicates the velocity component perpendicular to the fringes. This is equivalent to the result (4.12).

A typical LDA-signal, a Doppler burst, is shown in fig. 4.6. The high frequency is caused by the interference described above. The low frequency is due to the Gaussian intensity distribution of the laser beam and can be removed by a filter.

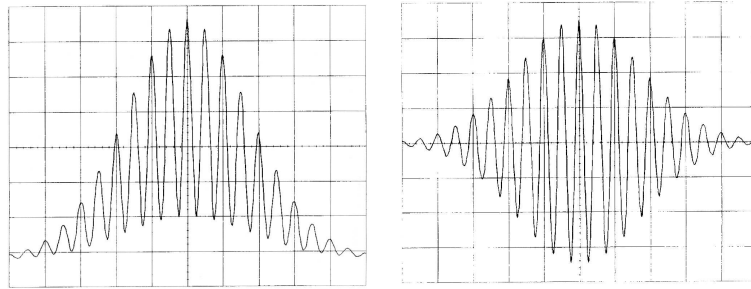


Figure 4.6: Doppler burst before and after passing the filter

A precise set up of the optical components is indispensable for correct measurement results. In the waist of a laser beam the wave fronts are plane. Intersection of two beams yields parallel fringes with constant fringe spacing. If the two laser beams do not intersect in their beam waists, the wave fronts are not plane but curved. The consequence can be seen in fig. 4.5(b). The fringe spacing is not constant anymore. As a consequence, wrong rms values are measured.

Strictly speaking this model is only valid for an infinitely small particle diameter. It is based on the light intensity at the position of the particle (interference fringes). However, the detection of the light intensity takes place at the photo detector. The intermediate step of the light being scattered by the particle is not taken into account. In the Mie-theory this intermediate step is taken into consideration (Adrian and Orloff [1], Durst *et al.* [13]).

Determination of the velocity direction

With the described LDA system it is not possible to detect the direction of velocity. A frequency shift in one of the laser beams is needed to render such a measurement possible. This leads to a movement of the interference fringes. The frequency $\Delta\nu_s$ of this movement is given by

$$\Delta\nu_s = \nu_{L,1} - \nu_{L,2} \quad (4.15)$$

where $\nu_{L,1}$ and $\nu_{L,2}$ are the frequencies of the two intersecting laser beams. Particles that pass the measuring control volume in the direction of the movement of fringes scatter light with a lower Doppler shift than the ones moving in opposite direction. In practice the movement of the fringe pattern is selected in such a way that it moves against the mean flow velocity with a speed higher than the highest velocity in reverse direction.

A possibility to change the frequency of laser light is the use of Bragg cells where the light is inflected on a acoustic wave traveling through the Bragg cell. The frequency of laser light is changed so that the frequency ν_s after passing the Bragg cell is given by

$$\nu_s = \nu_0 + m\nu_b \quad (4.16)$$

where $m = 0, \pm 1, \pm 2 \dots$ is the order of the refracted beam and ν_b the frequency of the acoustic wave. In the presented LDA measurements the refracted beams of 0^{th} and 1^{st} order are used. Since small frequency shifts can only be realized with huge Bragg cells, both laser beams are shifted with bigger but slightly different frequencies.

4.2.2 Residence Time Weighting

The sampling rate of the LDA system cannot be set to a fixed number but depends on the local and instantaneous flow field. Therefore, the LDA technique is characterized by random sampling times. Since the particles are carried into the scattering volume by the flow, it is wrong to assume the sampling and sampled processes to be independent (George *et al.* [21]). This creates a bias in the data if all realizations are treated equally. For uniformly seeded flow the number of particles that are carried with the flow at a higher velocity and thus remain in the measuring control volume for a shorter time is obviously higher than the number of slowly moving particles than can be detected in the same time interval. Therefore, the detected velocity will be too high.

The bias problem can be solved if the particles are distributed statistically uniformly in space. Then the signal can be treated as though it were sampled in space and not time. Most importantly the sampled process (the velocity) and the sampling process (the particle initial location) are statistically independent. It is straightforward (but very complicated) to show the unbiased statistics can be achieved if data is collected as long as a particle remains in the measuring control volume. Since the velocity of the particle is approximately constant while in the measuring volume, residence time weighting accomplishes this. A detailed discussion can be found in Buchave *et al.* [9].

The residence times Δt_j of the individual particles is used as a weighting factor for all measured moments. Thus the mean velocity is given by

$$\bar{U} = \frac{\sum_{j=1}^N (u_j) \Delta t_j}{\sum_{j=1}^N \Delta t_j} \quad (4.17)$$

and the n th central moment by

$$\frac{w^n}{w} = \frac{\sum_{j=1}^N (u_j - U)^n \Delta t_j}{\sum_{j=1}^N \Delta t_j} \quad (4.18)$$

where N is the total number of particles, u_j is the velocity and Δt_j the residence time of the j th particle.¹ Similar considerations must be applied to cross-correlations (or cross-spectra) as well, even if the used signal is continuous [21].

4.2.3 Particle Size

LDA measurements in air require the addition of seeding particles. The velocity of these particles is measured to determine the velocity of the fluid. Therefore, the particles have to have an inertia comparable to the one of a fluid element to be able to follow the high frequency oscillations of a turbulent flow field without slip.

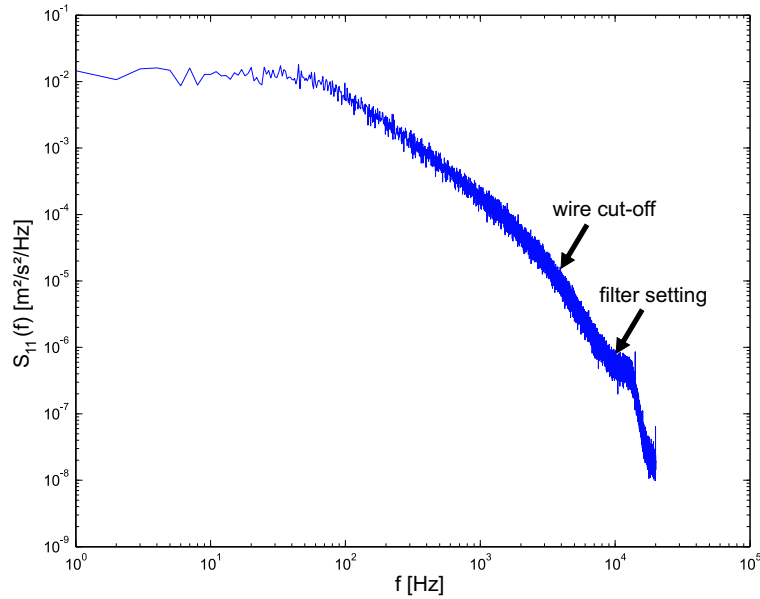
The dynamical behavior of a particle can be determined with the following equation (Durst *et al.* [13]).

$$\begin{aligned} \frac{\pi d_p^3}{6} \rho_p \frac{dU_p}{dt} = & -3\mu d_p V + \frac{\pi d_p^3}{6} \rho_f \frac{dU_f}{dt} \\ & - \frac{1}{2} \frac{\pi d_p^3}{6} \rho_f \frac{dV}{dt} - \frac{3}{2} d_p^2 \sqrt{\pi \mu \rho_f} \int_{t_0}^t \frac{dV}{dx} \frac{dx}{\sqrt{t-x}} \end{aligned} \quad (4.19)$$

One way of solving this equation of motion was presented by Hjelmfelt and Mockros [28]. For different density ratios between fluid and particle the maximum acceptable particle diameter for a certain frequency response can be determined. A table presenting such results is given in Durst *et al.* [13].

In this experiment the flow was seeded using SAFEX flow inside with a particle size that is claimed to have a number based size distribution around $0.7 \mu\text{m}$ where 73% of the particles are smaller than $1 \mu\text{m}$. With a density of $\rho_f = 1 \text{ kg/dm}^3$ those particles are comparable with the silicone oil presented in the table by Hjelmfelt and Mockros which was found to follow turbulent frequencies up to 10 kHz with an amplitude response of 99% for a particle diameter of $0.8 \mu\text{m}$. The powerspectrum at the furthest upstream position where the fastest fluctuations can be found is shown in fig. 4.7. The wire cut-off point is found significantly below 10 kHz. The filter settings that were set to 10 kHz were chosen so that the power spectrum showed no cut-off point. Thus the particle choice is adequate for this experiment.

¹Another technique to account for this measurement error is time interval weighting, where Δt_j is given by $(t_i - t_{i-1})$.

Figure 4.7: Power Spectrum at $x/D=30.3$

4.3 Combination of the Techniques

4.3.1 Simultaneous Operation of the Devices

In this experiment a single stationary hot wire, 1.25 mm long, and made of unplated $5\ \mu\text{m}$ tungsten wire was used. The probe was connected to a DANTEC Mini CTA and sampled with an IO Tech Wavebook 516 16 bit sample and hold A/D converter.

For the LDA measurements an argon laser was used. The optics were configured in back-scatter mode and the green component with a wave length of 514.5 nm was used for the measurements. With a front lens of focal length 0.6 m the calibration constant was 2.643 m/s/MHz. The beams, that emitted from the optical fiber with a diameter of 2.25 mm, were sent through two beam expanders and a focusing beam expander with expanding ratios of 1.94 and 1.55 respectively yielding a diameter of 13.13 mm at the front lens. The beam intersection was optimized by directing the beams through a pinhole in front of a light intensity detector. The angle between the intersecting beams was 11.17° yielding a measuring control volume of $30\ \mu\text{m}$ in diameter with a length of $300\ \mu\text{m}$. The processing hardware consisted of DANTEC BSA 57N11 Master that was operated in master coincidence mode.

The flow was seeded using a SAFEX Nebelgerät FOG 2001 smoke

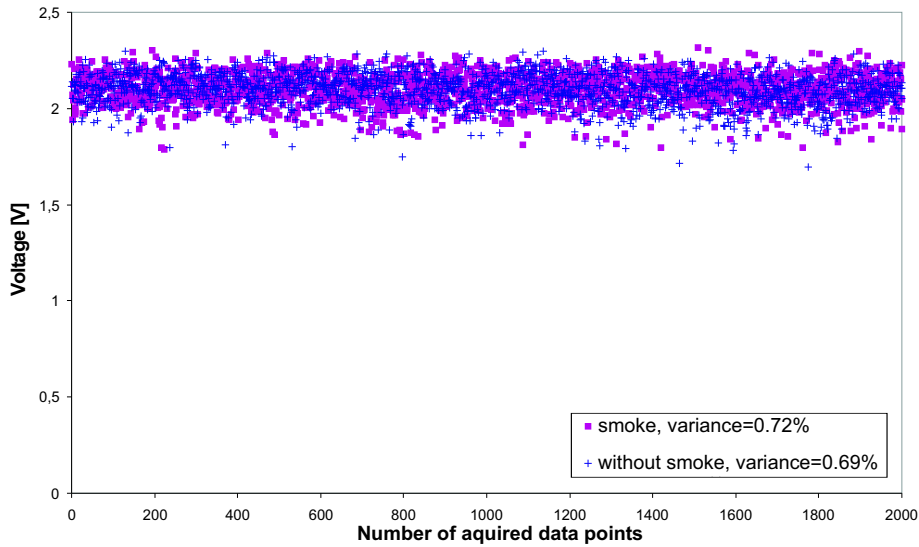


Figure 4.8: Effect of smoke on hot wire

generator operated with SAFEX Inside Nebelfluid Normal Power Mix.

In order to take simultaneous measurements with the different techniques it had to be ensured that the smoke required for the LDA measurements would not influence the HW in a negative way. Measurements with and without smoke were taken at the same position to see whether there was a substantial difference in the signal due to particle evaporation on the wire. The result of those measurements is shown in fig. 4.8. Clearly there is no significant difference between those signals. The variance for the obtained signal remains almost constant, suggesting strongly that particle evaporation on the wire is not a problem. This was of some concern since it might have interfered with the signal in such a way that higher voltage peeks (due to evaporation cooling) appeared.

The second possible problem with using the HW in smoke would have been a drift in the calibration due to depositions. Therefore, a calibration before and after a two hour operation in a smoke environment of the hot wire was taken. The difference of significantly less than 2% in the calculated velocity as can be seen in fig. 4.9 is similar to the drift of a hot wire operated under regular smokefree conditions for the same time.

4.3.2 Acquisition of Simultaneous Data

In order to calculate the spatial correlation between the HW and LDA sample it must be possible to match the two signals in time.

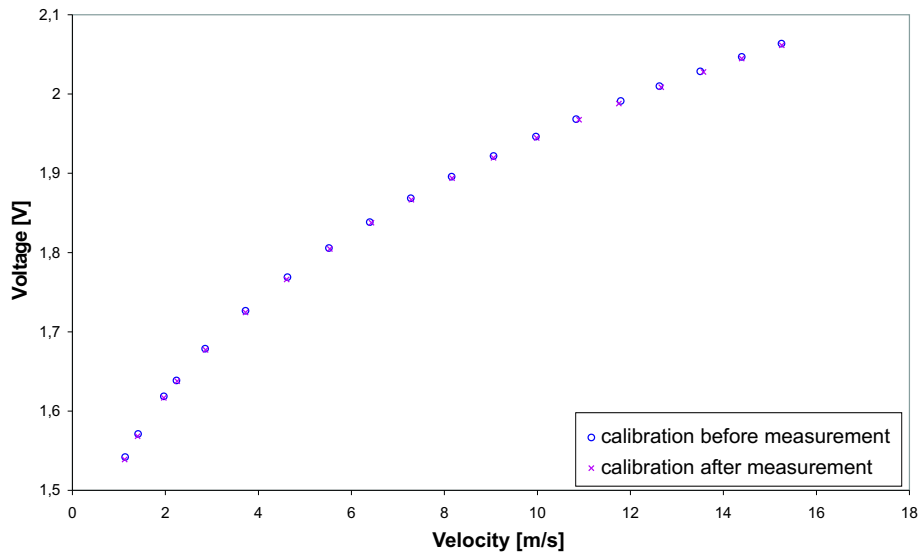


Figure 4.9: Calibration curves of the hot-wire before and after the use of smoke

The BSA provides a trigger signal when a measurement is started that is usually used for the synchronisation of two BSAs in multicomponent LDA measurements. This signal was taken out and used as an external TTL trigger for the IO Tech Wavebook ensuring simultaneous starting of the two measurements. Both the BSA and the Wavebook were connected to the same external clock to prevent a gradual time shift in the signals.

The BSA stores the number of counts from the external clock as arrival time information. Based on the external clock frequency, the actual arrival time can be calculated. Since the passing of particles through the measuring control volume is a random process, the BSA was set to sample for a certain time and not a certain number of bursts. The Wavebook was set to sample at a certain frequency and, when triggered by the BSA, started the CTA measurement at the same time. Until the total number of requested samples was reached, the Wavebook provided samples at equal time intervals. The exact time at which each sample was taken could thus be reconstructed from the number of samples taken up to that point and the sampling frequency.

At first the time records of the CTA were scanned for matches with the LDA arrival times. A matching was defined if the two samples happened to be within a time frame of $10 \mu\text{s}$. Using this technique only a rather low number of validated samples could be acquired. It was therefore decided to use all obtained LDA data by interpolating between the two surrounding

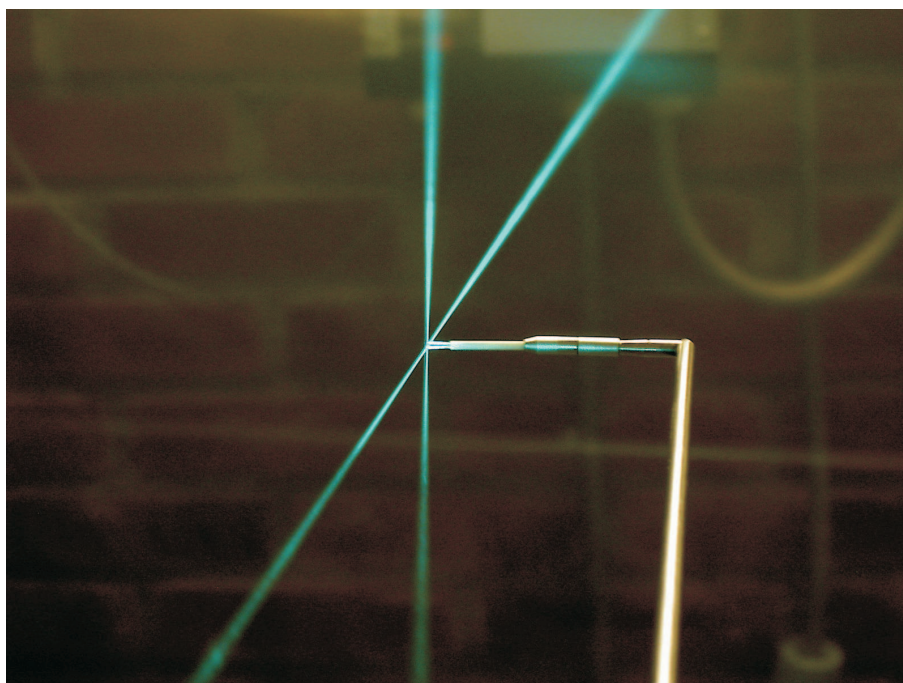


Figure 4.10: CTA and LDA measurement in the same position

CTA values linearly. This could be done since the data rate of the hot-wire anemometer was set high enough to satisfy the temporal Nyquist criteria for the filtered signal.

Fig. 4.10 shows a velocity measurement with the LDA measuring control volume and the hot-wire in the same position. The simultaneously obtained HW and LDA signals are plotted in fig. 4.11. While the hot-wire provides a continuous signal that is recorded at certain time intervals, the LDA samples arrive randomly. A signal is only present as long as a particle remains in the measuring control volume. Each of the vertical peaks representing a detected particle has a width that represents the particle's residence time, so that the higher peaks for faster particles are narrower than the peaks for slow traveling particles. The residence time of the particles however is too short to make the different residence times visible in the plot.

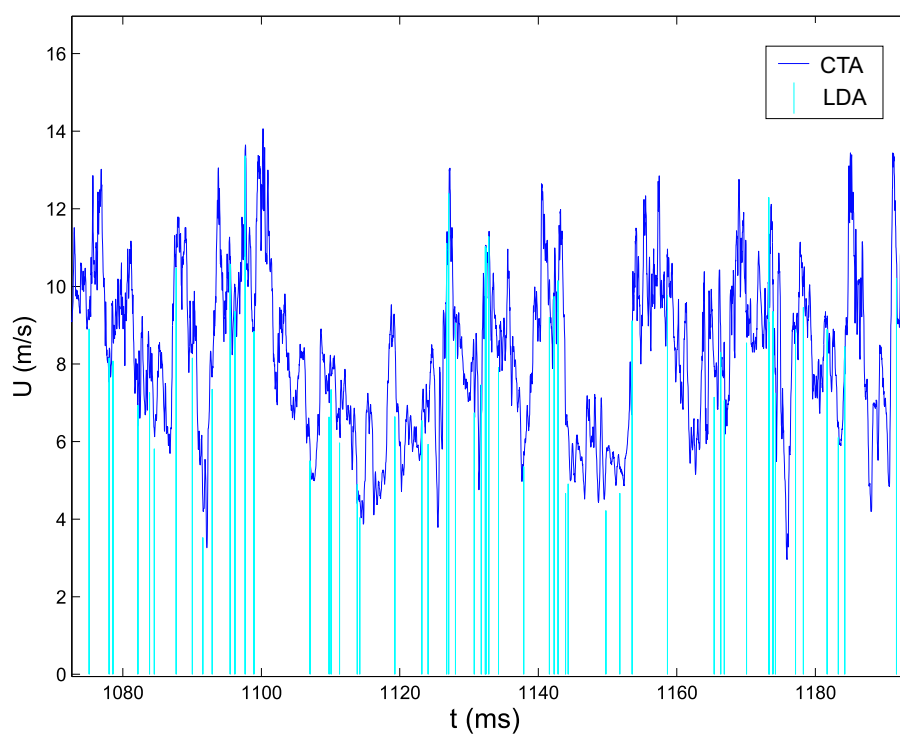


Figure 4.11: Simultaneous HW and LDA sampling

Chapter 5

The Experiment

The goal of this experiment was to verify the similarity analysis of the two-point velocity correlation tensor in the spatially developing axisymmetric jet. Therefore, a turbulent top-hat jet exhausting into a large room was investigated. Two-point correlation measurements at far downstream positions were performed using a combination of Constant Temperature Anemometry (CTA) and Laser Doppler Anemometry (LDA).

5.1 Experimental Set Up

In order to enable measurements at far downstream positions, a special facility was used in the experiment. The jet and enclosure were designed to be a 2/5-scale replication of the set-up used by Hussein *et al.* [31]. The jet, shown in fig. 5.1, was a cubic box ($58.5 \times 58.5 \times 59 \text{ cm}^3$) with an entrance for pressurized air on one side and an exit nozzle following a fifth order polynomial curve with a 1 cm diameter outlet on the other side. This jet was used earlier for the spanwise investigation of the far jet [19]. The jet was driven by a centrifugal blower yielding a maximum outlet velocity of 50 m/s. Measurements of the exit velocity were obtained from the exit nozzle via a silicon tube to a digital manometer.

The experimental set-up is shown in fig. 5.2. The jet itself was connected rigidly to the hot-wire and the laser traverse systems to ensure constant relative positions. The hot-wire traverse could be moved in the range of $x/D = 10$ to $x/D = 190$ covering the entire cross section of the jet at those positions. The LDA traverse provided only a comparatively small coverage in all three directions. The entire LDA traverse however could be moved along the x-axis. Both traverses were operated using computer controlled stepping motors yielding an accuracy in positioning of $10 \mu\text{m}$.

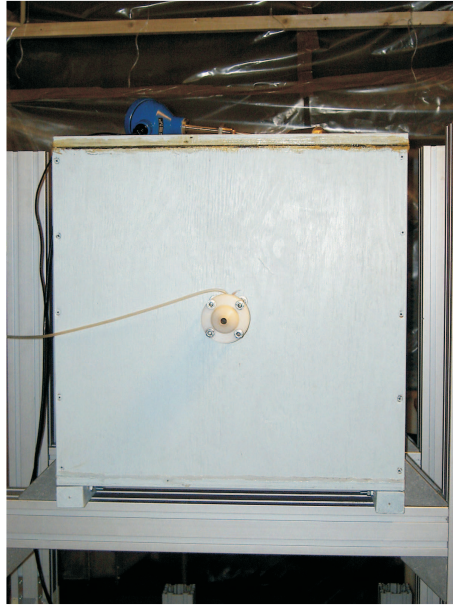


Figure 5.1: Measurement jet

Since the Constant Temperature Anemometer (CTA) required calibration before and after each measurement a second jet was used for calibration purposes. The measurement jet was not used for this procedure because of its small nozzle outlet. Measurements at far downstream positions required a calibration range down to 1 m/s and the volume flow rate to obtain such a low velocity was too small to obtain stable flow conditions at the outlet. Therefore, the jet used for calibration contracted only to a 9.8 cm outlet diameter following a 5th-order polynomial curve. It was driven by a centrifugal blower yielding stable outlet velocities of up to 25 m/s and down to 1 m/s. This jet was extensively used in the past by the Turbulence Research Laboratory in Buffalo. It was used to study the far field of the axisymmetric jet before. A thorough description can be found in Gamard [20].

5.2 The Enclosure

In order to provide uniform spatial seeding for the LDA measurement the jet facility was enclosed. This enclosure of the jet had to be big enough to ensure that the jet truly behaved like a free jet in the investigated area. Capp [10] and Hussein *et al.* [31] investigated this problem and proposed a criterion to design the enclosure in such a way that the jet remains undisturbed by the



Figure 5.2: Picture of the experimental set up

walls. The following discussion is summarized from Appendix B of Hussein *et al.* [31].

A jet emerges from a mass and momentum source and spreads while developing downstream by entraining mass from the outside. The initial mass flow is comparatively small to the mass flow added to the jet through entrainment. Especially at large distances downstream it can be argued that the initial mass flow can be neglected. The walls at a certain radius cause the entrainment to be fed by a reverse flow outside the jet. The momentum of this return flow contributes a positive momentum to the momentum integral. Thus, while evolving downstream, the jet is progressively modified from a jet at infinite environment.

At every cross section of the enclosure mass must be conserved so the return flow must balance the jet flow itself, so that

$$\int \int_{jet} U dA = \int \int_{return} U dA. \quad (5.1)$$

Assuming the flow to be uniform across the cross-section and the area taken up by the jet to be significantly smaller than the one taken up by the return

flow, the left side of mass conservation can be rewritten as

$$\int \int_{jet} U dA = U_R A_R \quad (5.2)$$

where U_R is the return flow velocity at a given x -location (assumed to be uniform) and A_R is the cross-sectional area of the room at this position.

Since the only momentum added to the jet is at the source (a unique feature of a jet), the momentum integral at each cross-section of the room must be equal to the rate at which momentum is added at the source. Considering the flow to consist of a jet-like part and a return flow yields the following momentum constraint

$$\int \int_{jet} U^2 dA + \int \int_{return} U^2 dA = M_0. \quad (5.3)$$

This equation can be approximated with the same assumption made for mass conservation yielding

$$\int \int_{jet} U^2 dA + U_R^2 A_R = M_0. \quad (5.4)$$

A typical velocity profile in similarity-like variables using the local jet momentum integral can be described as

$$U = BM^{\frac{1}{2}} x^{-1} f(\eta) \quad (5.5)$$

where

$$M(x) \equiv \int \int_{jet} U^2 dA. \quad (5.6)$$

and

$$\eta = \frac{r}{x}. \quad (5.7)$$

Choosing a Gaussian profile for the profile function $f = (\eta)$ yields the local momentum ratio as

$$\frac{M}{M_0} = \left[1 + \frac{16}{\pi B^2} \frac{x^2}{D} \frac{A_0}{A_R} \right]^{-1} \quad (5.8)$$

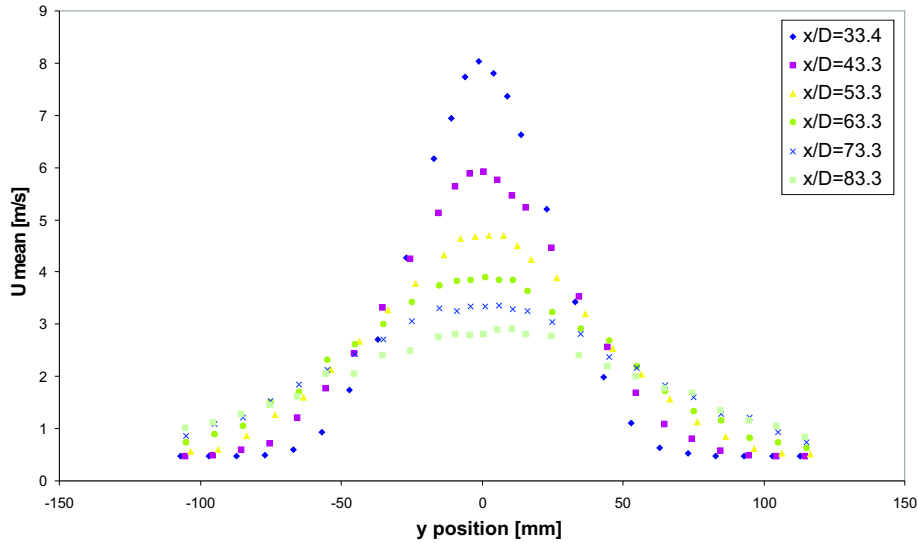


Figure 5.3: Velocity profiles at different downstream positions

where D is the jet exit diameter ($A_0 = \frac{1}{4}\pi D^2$) and A_R is the cross section of the room.

The enclosure in this experimental set up is a 2/5 scale version (based on jet outlet diameter and room width) of the enclosure used for the jet measurements performed at the the Turbulence Research Laboratory at the State University of New York at Buffalo (Hussein *et al.* [31]) where the jet was found to retain 99% of its original momentum up to a downstream distance of 70 diameters. In this setup the enclosure had a cross section of $2 \times 2 \text{ m}^2$. In comparison to the jet outlet the enclosure's cross section was bigger by a factor of 10^4 . The distance between the jet exit and the end wall was made as large as possible with a length of 9.6 m, in scaled variables a factor of 2 longer than in Buffalo.

5.3 Properties of the Jet

After the set up of the experimental facility the general characteristics of the turbulent free jet were determined. With an outlet speed of 40 m/s the Reynolds number was higher than 26,000. Using HWA, velocity profiles of the jet were measured at different downstream positions. The centerline was found by scanning the jet in y - and z - direction. The results of those measurements are shown in fig. 5.3 to fig. 5.5. The mean velocity profiles show the decay of the centerline velocity and the spreading of the jet as

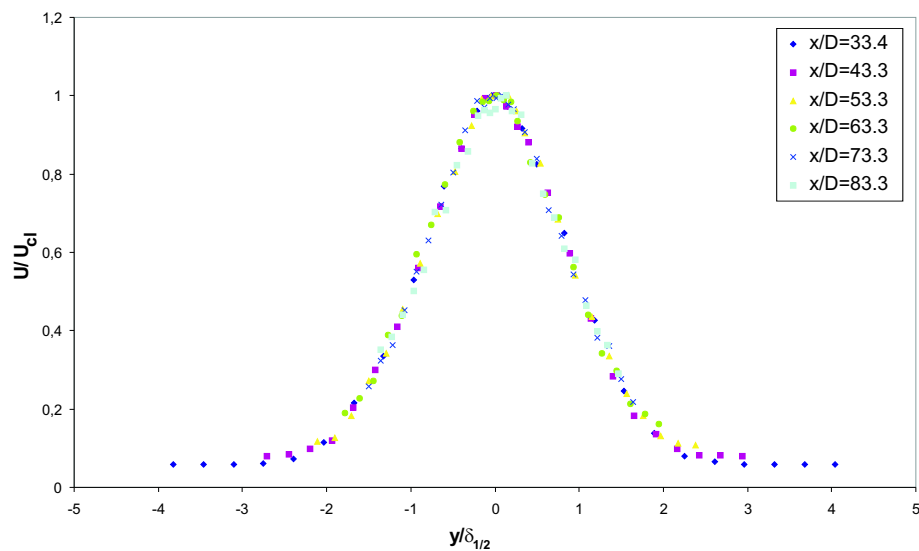


Figure 5.4: Normalized velocity profiles

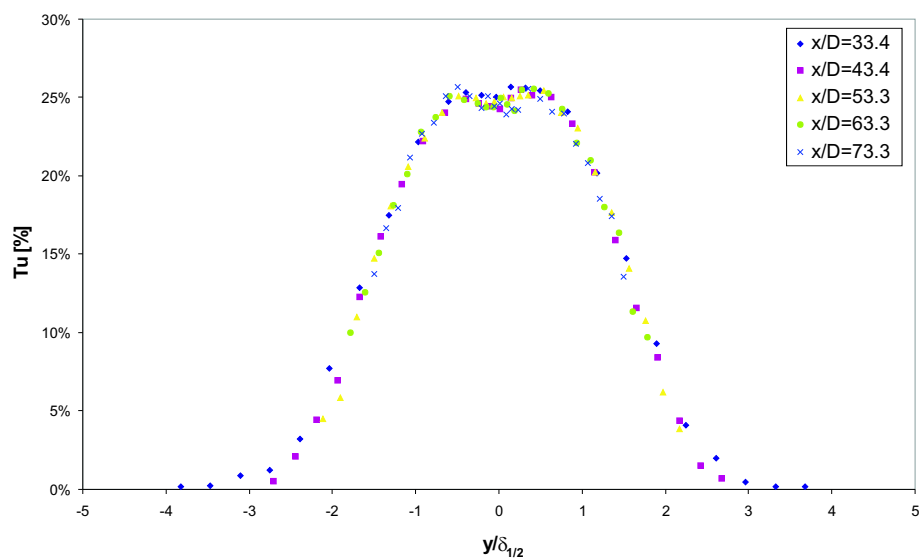


Figure 5.5: Turbulence intensity plotted against normalized radial position

one moves further downstream. Scaling the measured quantities with the centerline velocity and the jet half width respectively yields a collapse of all the profiles. The same behavior can be found for higher order moments, so that the turbulence intensities at different downstream position collapse if plotted against $y/\delta_{1/2}$.

For a self-preserving jet, the centerline velocity is given by

$$U_c = \frac{BM_0^{\frac{1}{2}}}{x - x_0} \quad (5.9)$$

where x_0 represents a virtual origin and B is a constant. Taking into consideration that the jet has a top-hat profile, the momentum flux $\rho_f M_0$ can be determined using the jet exit velocity U_0 and the exit diameter D .

$$\rho_f M_0 = \frac{1}{4}\pi U_0^2 D^2 \quad (5.10)$$

Substituting this into equation 5.9 yields

$$\frac{U_0}{U_c} = \frac{1}{B_u} \left[\frac{x}{D} - \frac{x_0}{D} \right]. \quad (5.11)$$

where the constants are related by

$$B_u = \frac{1}{2}\pi^{\frac{1}{2}}B. \quad (5.12)$$

Thus the virtual origin as well as the constant B_u can be obtained by plotting U_0/U_c as a function of the axial location. The centerline HW velocity measurements yielded a virtual origin of $x_0 = 4.6D$ and a decay constant of $B = 6.5$ (fig. 5.6). These can be compared with the HWA results from Hussein *et al.* [31] for which $B = 6.7$ and $x_0 = 2.7D$. Note that these are somewhat different from the residence time weighted LDA results also obtained by Hussein *et al.* which are more accurate. They do confirm, however, that this jet is behaving in the expected manner, and the slight differences are consistent with the expected effects of the upstream conditions. The virtual origin x_0 can also be determined by plotting the halfwidth of the jet against the axial position as it is shown in fig. 5.7. In this plot the virtual origin is found to be $x_0 = 4.5D$ which agrees with the above result. The growth rate constant for the jet is represented by the slope of the curve. Since the halfwidth $\delta_{1/2}$ is plotted, the double of the given slope is the actual growth rate constant A for this jet, which is therefore given by $A \approx 2$.

With the obtained values it is possible to determine the influence of the enclosure. Equation 5.8 describes the conservation of momentum at different

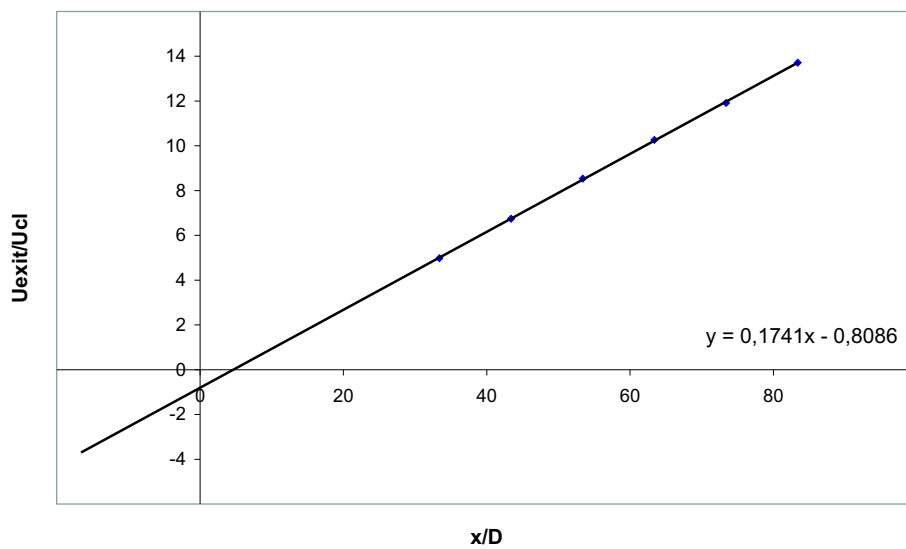


Figure 5.6: Determination of the virtual origin x_o and the decay constant B

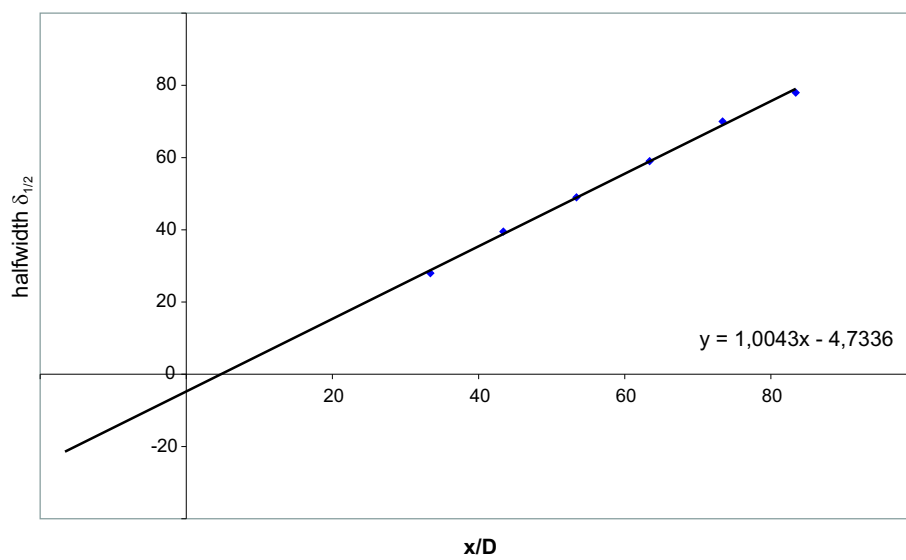


Figure 5.7: Determination of the virtual origin x_o and the growth rate of the jet

downstream positions as

$$\frac{M}{M_0} = \left[1 + \frac{16}{\pi B^2} \frac{x^2}{D} \frac{A_0}{A_R} \right]^{-1}$$

where A_0 is the outlet area of the jet and A_R is the area of the room at the considered downstream position. For this specific set-up 99% of the momentum is retained until 80 diameters downstream.

5.4 Spatial Correlation Measurements

Since the hot-wire traverse had a better alignment with the jet, the centerline was determined based on the hot-wire measurement. The exact position of the laser was determined by moving the measuring control volume to the same position as the hot wire. When both of the laser beams showed scattering effects due to the interference with the hot-wire, the position of the two devices was assumed to be the same. Thus the relative positioning error can be estimated as a typical measuring volume diameter. Note that while this procedure would not be accurate enough for the determination of the microscales, it was more than adequate for the determination of the correlation functions at large separations which was the primary focus of this experiment.

The constellation of the LDA measuring control volume and the hot wire during a measurement with the smallest separation is shown in fig. 5.8. For measurements at larger separations the hot wire was gradually moved as schematically demonstrated in fig. 5.9. Two-point correlations in the longitudinal direction were measured using reference positions of 30.3, 43.3 and 53.3 diameters downstream.

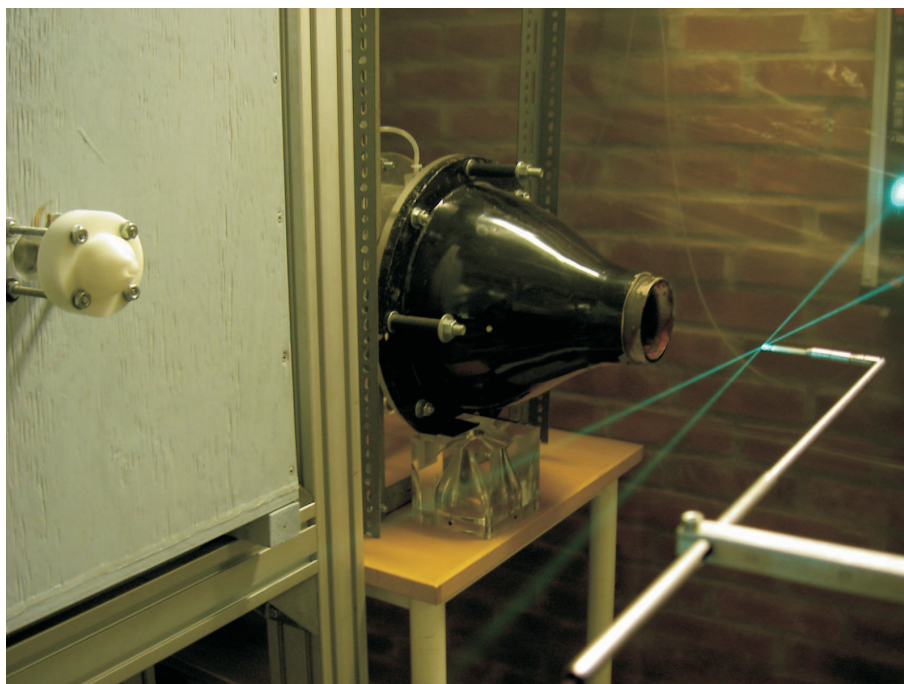


Figure 5.8: Set-up during a measurement

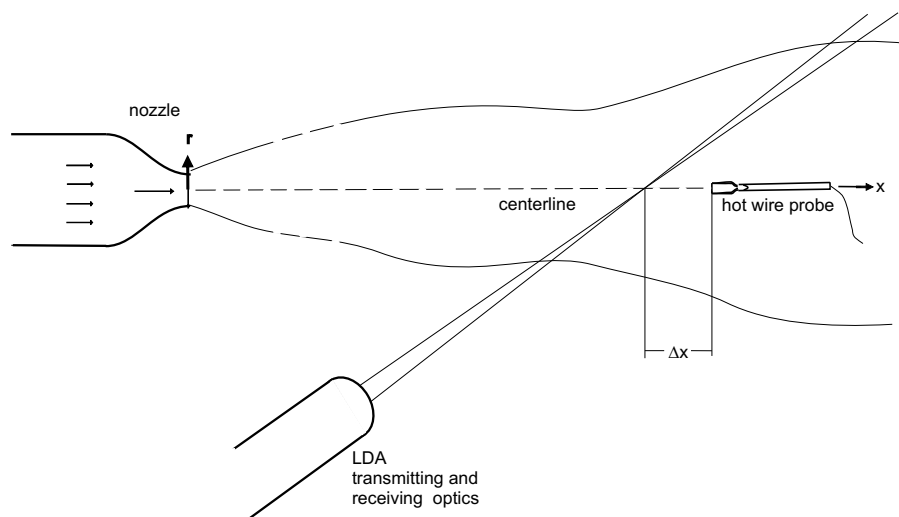


Figure 5.9: Schematic set-up of hot wire and LDA during a measurement

Chapter 6

Measurement Accuracy

6.1 Preliminary Measurements

At first mean velocity profile measurements were performed with CTA and LDA separately. Fig. 6.1 shows the comparison between HWA and LDA measurements at the same position. It can clearly be seen that the HW measures higher velocities. This is due to the high turbulence intensity in this flow such that radial velocity fluctuations lead to increased heat transfer from the wire yielding biased results. The effect of high turbulence intensities on HW measurements has been discussed by a number of authors including Tutu and Chevray [42], Beuther *et al.* [7] and Hussein *et al.* [31]. The latter reported measurements of the turbulent velocity field of an axisymmetric jet with hot wires in comparison with flying hot wires and LDA. The HW results differed substantially from the results obtained using the two other techniques. Those deviations were at a minimum along the centerline where the local turbulence intensity is lowest. Curve fits for both the HW and the LDA velocity profiles were presented. Those curves in comparison with the data taken in this experiment are shown in fig. 6.2. The measured deviations between the LDA and HW measurements are smaller than those predicted by Hussein *et al.* but show the same trend up to a scaled radial position of 0.13. The collapse of the HW and LDA data beyond that point is not found in this work, on the contrary the deviation increases. This discrepancy may simply reflect different initial conditions in the two experiments.

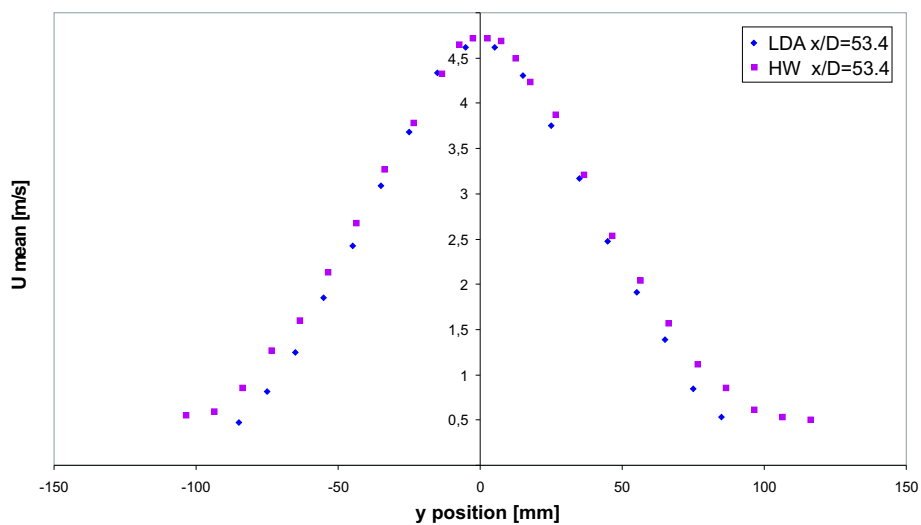


Figure 6.1: HW and LDA measurements at the same positions

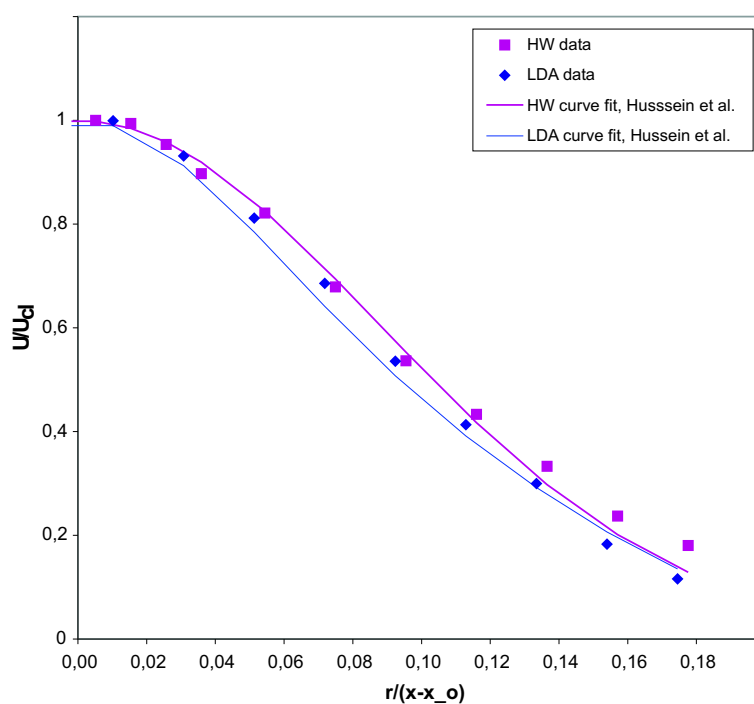
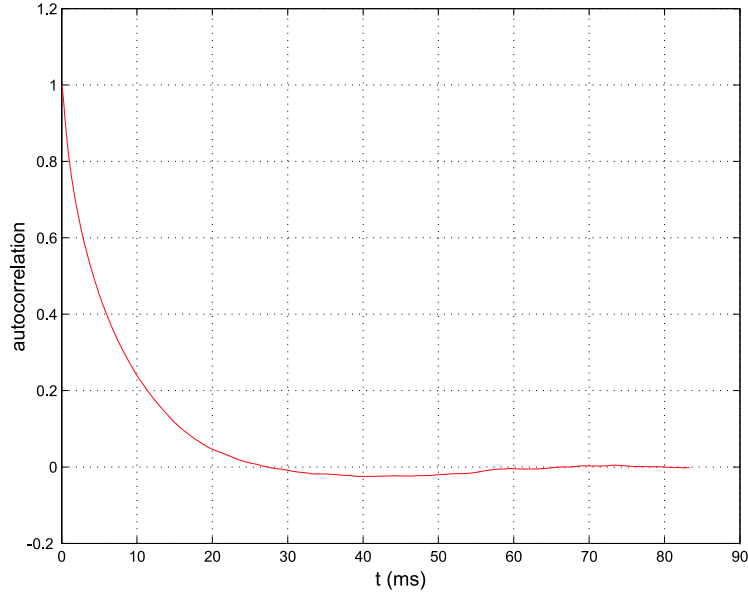


Figure 6.2: Comparison with the curve fits obtained by Hussein *et al.* [31]

Figure 6.3: Autocorrelation at $x/D = 53.3$

6.2 Operating Conditions

6.2.1 Measuring Time

First, the autocorrelation $\rho(\tau)$ was determined at every downstream reference position where

$$\rho(\tau) = \frac{\overline{u(t)u(t+\tau)}}{\text{var}(u)}. \quad (6.1)$$

The integral of the autocorrelation over positive values of τ yields the integral time scale; i.e.

$$I_t = \int_0^{\infty} \rho(\tau) d\tau. \quad (6.2)$$

To ensure statistical independence only one sample every two integral time scales is required. Further downstream where the integral time scale is larger a longer record period T is necessary to obtain the same accuracy. The number of statistically independent samples N is thus given by

$$N = \frac{T}{I_t}. \quad (6.3)$$

6.2.2 Hot Wire Settings

The filter settings of the HWA were chosen so that no cut off point was visible in the power spectrum meaning that spatial resolution (wire cut-off) was the dominant limitation on the frequency response. To capture the fastest present fluctuations the data rate of the HW was set to four times the filter settings, substantially higher than the temporal Nyquist criterion.

6.2.3 Seeding

For bias-free LDA measurements, statistically uniform spatial seeding was required. Since the seeding could not be dosed in tiny amounts, continuous seeding was not a possibility. Therefore, the room was filled with smoke prior to a measurement using the jet to distribute the particles. After about 45 minutes the seeding level had been reduced in such a way that the BSA encountered a sampling rate of less than 600 Hz. The upper limit of 600 Hz is set by the buffer capacity of the BSA. Measurements were taken until the sampling rate had dropped to about 150 Hz, a number higher than one sample every two integral time scales. This span allowed measurements for approximately 30 minutes.

6.3 Spatial Correlation

The average velocity $U_{mean,LDA}$ as well as the variation $u_{rms,LDA}$ obtained from the LDA were corrected using the residence time weighting technique as explained in chapter 4.2.2. In the determination of the correlation this effect is also accounted for and the fluctuating part of the LDA signal is weighted by the measured residence time Δt of each scattering particle. Thus, the spatial correlation is estimated using

$$C(x, x') = \frac{\sum_{n=0}^N (u_{HW,n}(x') u_{LDA,n}(x) \Delta t_n)}{\sqrt{u_{rms,HW}^2(x') u_{rms,LDA}^2(x) \sum_{n=0}^N (\Delta t_n)}} \quad (6.4)$$

where $u_{HW/LDA}$ is the fluctuating part of the HW and the LDA signal respectively given by

$$u = U_m - U_{mean} \quad (6.5)$$

and Δt_n is the residence time of the n^{th} particle. The relative error ϵ can be defined as

$$\epsilon^2 = \frac{var(C - \bar{C})}{\bar{C}^2} \quad (6.6)$$

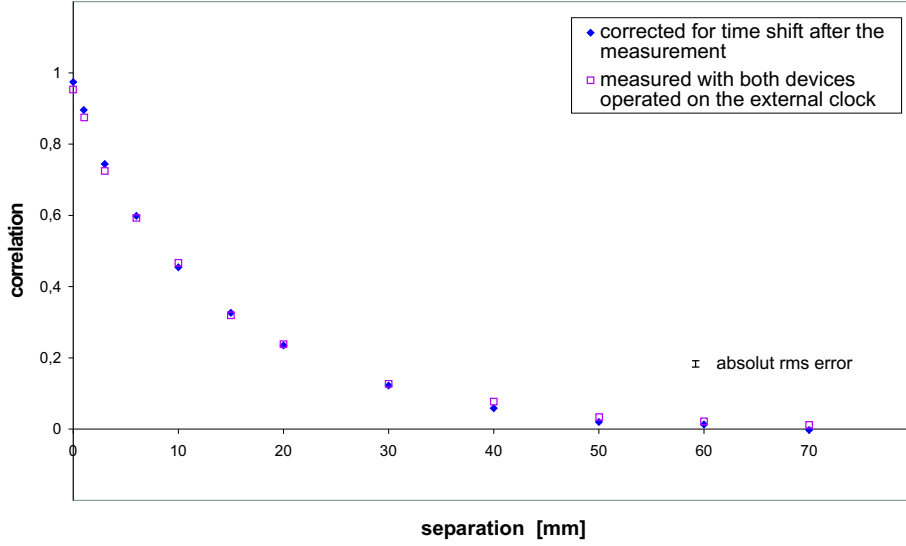


Figure 6.4: Comparison between measurement on external and internal clock (corrected for time shift)

where C is the estimated value of the correlation and \overline{C} is its expected value. It can be shown by assuming the velocity to be jointly normal and the correlation exponential (George [21]) that

$$\epsilon^2 = \frac{1}{N} C^{-2}. \quad (6.7)$$

Thus the smaller C is, the greater the number of samples required to achieve a given statistical accuracy. Note that since ϵ^2 varies with C^{-2} , the absolute statistical error is the same at all separations, i.e. at all values of C .

The settings at each positions and the resulting errors for different correlation coefficients C are summarized in the following table.

x/D	30.3	43.3	58.3
integral time scale [ms]	3.5	8.5	14
low pass filter settings [kHz]	10	10	3
HW sampling rate [kHz]	40	40	12
total record time [s]	300	300	600
number of statist. independent samples	85714	17647	21429
relative error ϵ [%] for $C = 1.0$	0.3	0.8	0.7
relative error ϵ [%] for $C = 0.5$	0.7	1.5	1.4
relative error ϵ [%] for $C = 0.1$	3.8	7.5	6.8

After the first measurements it was detected that the IO Tech Wavebook used for the HW data acquisition was not running on the external clock but on its internal one instead. The resulting time shift was determined by recording the HW and the LDA signal simultaneously for 10 minutes. The obtained correction factor was thereafter applied to sampling records of 30 seconds to max. 2 minutes. With the fixed data acquisition system the correlation measurement at $x/D = 30.3$ was retaken. The result can be seen in fig. 6.4. The correction factor applied to the first measurement was clearly accurate enough to nullify the error introduced due to the operation on different clocks. The difference between the obtained correlation lies within the statistical error.

6.4 Effect of Hot-Wire Errors

As discussed earlier the velocity measured by the HW is higher than the actual one because the fluctuating radial component also contributes to the cooling of the wire. The influence of this erroneous measurement on the calculated correlation is discussed in the following.

The instantaneous velocity detected by the HW, say \tilde{U}_m is given by

$$\tilde{U}_m = \sqrt{(\bar{U} + u)^2 + v^2} = \bar{U} \sqrt{1 + 2\frac{u}{\bar{U}} + \frac{u^2}{\bar{U}^2} + \frac{v^2}{\bar{U}^2}}. \quad (6.8)$$

Substituting for the square root by the series expansion

$$f = \sqrt{1+x} = 1 + \frac{1}{2}x - \frac{1}{4}\frac{1}{2!}x^2 + \frac{3}{8}\frac{1}{3!}x^3 - \frac{15}{16}\frac{1}{4!}x^4 + \dots \quad (6.9)$$

and carrying the calculation through with an accuracy of 4th order yields

$$\tilde{U}_m = \bar{U} \left[1 + \frac{u}{\bar{U}} + \frac{1}{2}\frac{v^2}{\bar{U}^2} - \frac{1}{2}\frac{uv^2}{\bar{U}^3} + \frac{1}{2}\frac{u^2v^2}{\bar{U}^4} - \frac{1}{8}\frac{v^4}{\bar{U}^4} + O(5) \right]. \quad (6.10)$$

The fluctuating quantity which is used to calculate the correlation is given by

$$u_m = \tilde{U}_m - \bar{U}_m \quad (6.11)$$

$$u_m = u + \frac{u}{\bar{U}} + \frac{1}{2}\frac{v^2}{\bar{U}} - \frac{1}{2}\frac{\overline{v^2}}{\bar{U}} - \frac{1}{2}\frac{uv^2}{\bar{U}^2} + \frac{1}{2}\frac{\overline{uv^2}}{\bar{U}^2} + \frac{1}{2}\frac{u^2v^2}{\bar{U}^3} - \frac{1}{2}\frac{\overline{u^2v^2}}{\bar{U}^3} - \frac{1}{8}\frac{v^4}{\bar{U}^3} + \frac{1}{8}\frac{\overline{v^4}}{\bar{U}^3}. \quad (6.12)$$

Say the LDA detects the fluctuating quantity $u(x)$ and the hot wire $u_m(x')$. The product of those two averaged in time is given by

$$\overline{u(x)u_m(x')} = \overline{u(x)u(x')} + \frac{1}{2}\frac{\overline{u(x)v^2(x')}}{\bar{U}(x')} - \frac{1}{2}\frac{\overline{u(x)uv^2(x')}}{\bar{U}^2(x')} + \dots \quad (6.13)$$

The leading term causing the error in the measurement can be rewritten as

$$\overline{u(x)v^2(x')} = C_{u,v^2} u_{rms}(x) v_{rms}^2(x'). \quad (6.14)$$

For zero separation the variance in v direction is about half the variance in u direction along the centerline (Hussein *et al.* [31]), so that

$$\overline{u(x)v^2(x)} = C_{u,v^2} \frac{1}{2} u_{rms}^3. \quad (6.15)$$

Plugging this into equation 6.13 yields

$$\overline{u^2(x)} = \overline{u(x)u_m(x)} - \frac{1}{2\overline{U}(x)} C_{u,v^2} \frac{1}{2} u_{rms}^3(x). \quad (6.16)$$

The relative error in the measurement is thus given by

$$\frac{\overline{u(x)u_m(x)} - \overline{u^2(x)}}{\overline{u^2(x)}} = \frac{1}{2\overline{U}(x)} C_{u,v^2} \frac{1}{2} u_{rms}(x). \quad (6.17)$$

The turbulence intensity along the centerline is $Tu = \frac{u(x)}{\overline{U}(x)} = 0.25$ and the correlation coefficient C_{u,v^2} can never exceed the maximum value of 1. In fact it is much lower than that. The measurements of Hussein *et al.* [31] show the third order moment to be in the order of 0.002 which is equivalent to a correlation coefficient of 0.1 so that the relative error in the correlation introduced by the falsified hot-wire measurement is below 1%.

Chapter 7

Results

7.1 Two-Point Correlations

Spatial correlations along the centerline were measured using reference points of 30.3, 43.3 and 53.3 diameters downstream. The measuring time for each of the two upstream reference points was set to 300 s and 600 s for the reference point furthest downstream. With the repeated seeding of the room and HW calibrations, the data acquisition for one correlation curve took about 2 days.

Fig. 7.1 shows the measured spatial correlations. The point that is referred to as zero separation is in fact measured with a separation about 50 μm since it was not possible to place the HW within the measuring volume of the LDA without disturbing its signal. Clearly the two-point correlation dies off more slowly with increasing distance downstream. Thus the streamwise turbulence scales are growing as the shear layer itself grows, as expected. Due to the high number of statistically independent samples the absolute rms-error is very small.

The measuring point marked with a question mark shows a much higher correlation as expected for this position. The data was acquired in 5 blocks of 2 minutes at this position, and showed a variance in the obtained correlation of only $3.6 \cdot 10^{-5}$. Therefore the deviation is not related to the statistical error. It might be due to an eddy shed by the hot wire traversing system but no definite explanation for this offset can be given at this time.

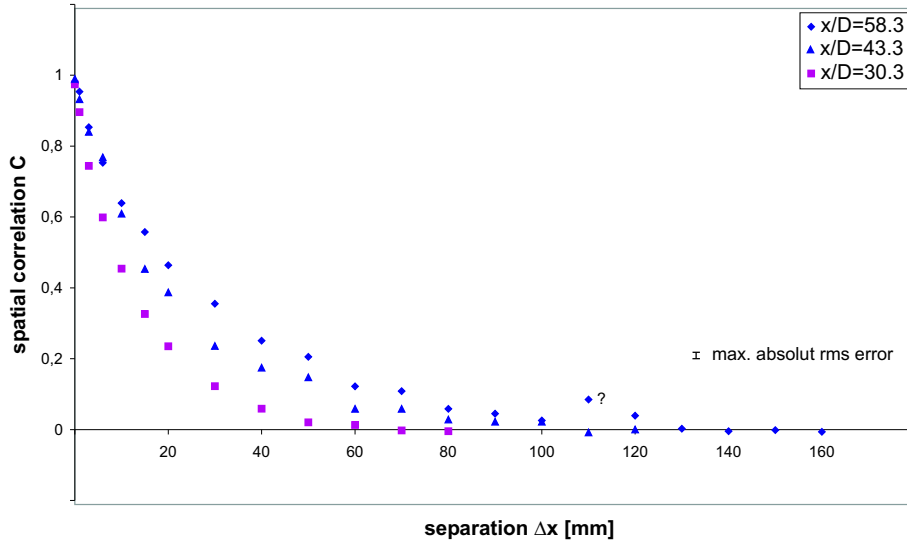


Figure 7.1: Two-point correlations at different downstream positions

7.2 Scaled Two-Point Correlations

The transformed coordinate for the x -direction as proposed by Ewing [15] is given by

$$\xi = \ln \left(\frac{x - x_0}{l} \right). \quad (7.1)$$

In this experiment the virtual origin x_0 was found using the decay of the centerline velocity to be $4.64D$. The arbitrary length scale l was chosen to be the outlet diameter D of the jet.

If the LDA measurement is taken at position x while the HW measures at position x' and each of those positions is separately transformed into the new coordinates ξ and ξ' , the theory predicts a collapse of the correlation curves if plotted against $\xi' - \xi$. This is tantamount to a transformation of the velocity field in x -direction into a homogeneous field where the correlation between two points depends on their separation only and not on their absolute positions. Fig. 7.2 shows the measured correlations in the proposed scaling. The point that stood out in the unscaled correlation curves is still clearly visible. From this plot it is obvious the correlation curves indeed collapse if scaled in similarity variables, exactly as predicted.

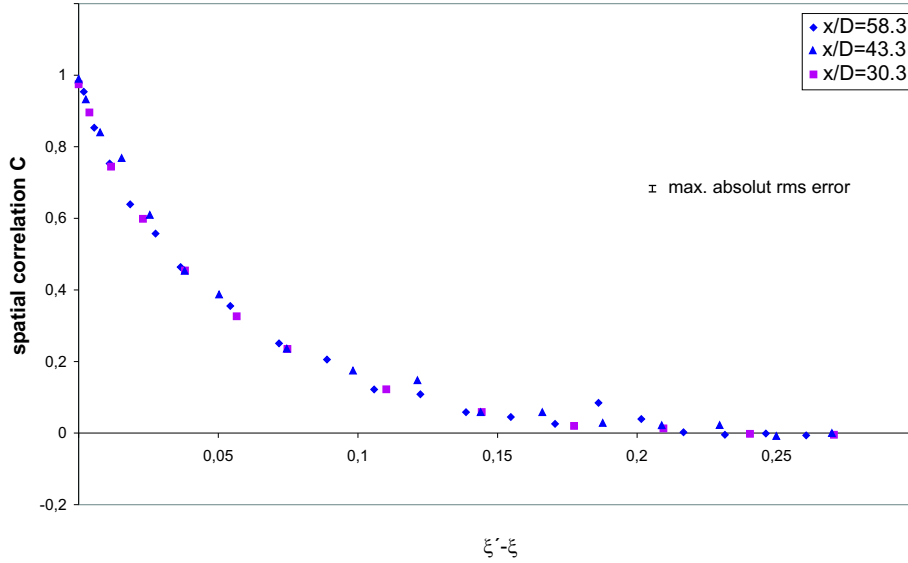


Figure 7.2: Two-point correlations in similarity variables

7.3 Taylors Frozen Field Hypothesis

Taylors Frozen Field Hypothesis (FFH) [40] implies that space correlations can be determined from time correlations when the turbulent eddies are convected past the observation point so fast that they do not undergo substantial changes during their passage.

The basic idea is that the substantial derivative of a "frozen" particle is zero,

$$\frac{D}{Dt} = 0. \quad (7.2)$$

For a one-dimensional, steady, non-turbulent flow this can be rewritten to apply to a point in the flow field as

$$\frac{\partial}{\partial t} = U \frac{\partial}{\partial x} \quad (7.3)$$

or

$$\frac{\partial}{\partial t} - U \frac{\partial}{\partial x} = 0. \quad (7.4)$$

This condition is approximately fulfilled for low turbulence intensities

$$\frac{u}{U} \ll 1 \quad (7.5)$$

and if the scales are sufficiently small, so the flow does not evolve significantly as it is swept past the point of interest. In flows with high turbulence intensities FFH is usually not applicable because of the fluctuating convection velocity effect (Lumley [35]). For example a certain wavenumber k is not converted to a single frequency f by

$$f = \frac{U_{con}}{2\pi}k \quad (7.6)$$

but due to the fluctuating convection velocity U_{con} is represented by a frequency band whose width is given by

$$\Delta f = \frac{u}{U_{con}}f \quad (7.7)$$

where u is the fluctuating component of the velocity.

Nevertheless, FFH was applied to the data set obtained in these measurements. The temporal autocorrelation ρ at downstream positions of 30.3, 43.3 and 53.3 was calculated based on HW data from those positions. The time lag τ was transformed into a spatial separation Δx^* by

$$\Delta x^* = \tau U_c. \quad (7.8)$$

where the centerline velocity U_c was chosen to be the convection velocity of the flow field. The result of this transformation in comparison with the measured spatial correlation is shown in fig. 7.3.

The agreement of the obtained curves is surprising: The transformed autocorrelations almost perfectly match the measured spatial correlations. It appears as if it is possible to apply Taylor's FFH to this flow of high turbulence intensities, at least for measurements along the centerline. The separation of the transformed autocorrelation curves were also rescaled according to Multi-Point Similarity. For an autocorrelation measured at position x , the separation in similarity variables $\psi' - \psi$ is given by

$$\psi' - \psi = \ln \frac{x^{*'}}{x^*} \quad (7.9)$$

where

$$x^* = x - x_0 \quad (7.10)$$

and

$$x^{*'} = (x - x_0) + \Delta x^*. \quad (7.11)$$

Fig. 7.4 shows the measured correlation as well as the transformed autocorrelation curves in similarity variables. The transformed autocorrelations seem to show an even better collapse than the spatial correlation.

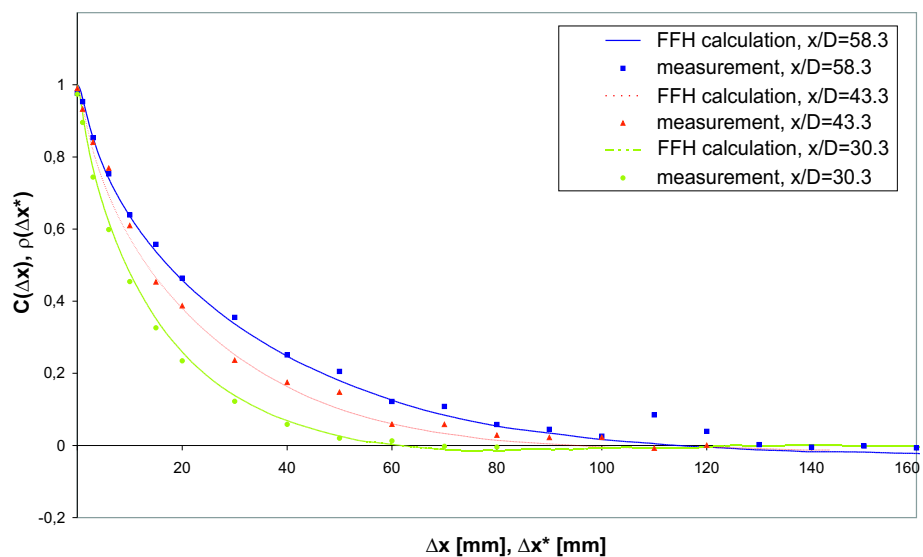


Figure 7.3: Spatial correlations in comparison with transformed autocorrelations

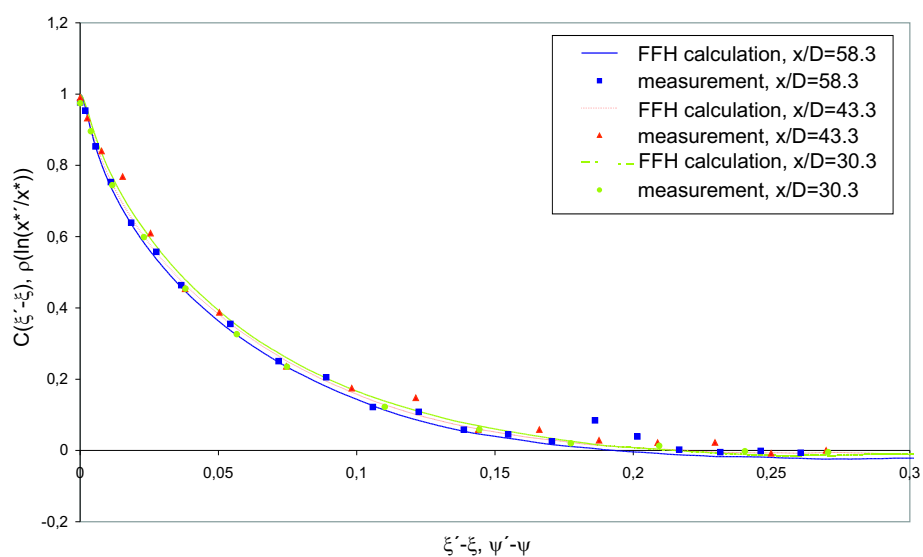


Figure 7.4: Spatial correlations and transformed autocorrelations in similarity variables

7.4 Implication of Taylor's Hypothesis and Similarity for Spectra

If Taylor's hypothesis can be applied to this flow, it should also be applicable to the frequency and (FFH) wavenumber spectra. The frequency spectrum is given by

$$S_{11}(f) = \int_{-\infty}^{\infty} e^{-i2\pi f\tau} B_{11}(\tau) d\tau. \quad (7.12)$$

For zero frequency this can be rewritten as

$$S_{11}(0) = \int_{-\infty}^{\infty} B_{11}(\tau) d\tau = 2\overline{u^2}I_t \quad (7.13)$$

where I_t is the integral time scale that can thus be expressed as

$$I_t = \frac{S_{11}(0)}{2\overline{u^2}}. \quad (7.14)$$

The same transformation can be performed for the wavenumber spectrum.

$$F_{11}^1(k) = \frac{1}{2\pi} \int_{-\infty}^{\infty} e^{-ikr} B_{11}(r) dr \quad (7.15)$$

$$F_{11}^1(0) = \frac{1}{2\pi} \int_{-\infty}^{\infty} B_{11}(r) dr = \frac{2}{2\pi} \int_0^{\infty} B_{11}(r) dr = \frac{\overline{u^2}}{\pi} \int_0^{\infty} \rho_{11}(r) dr = \frac{\overline{u^2}}{\pi} L_{11} \quad (7.16)$$

The spatial integral scale L_{11} is thus given by

$$L_{11} = \frac{\pi}{\overline{u^2}} F_{11}^1(0). \quad (7.17)$$

If FFH is applicable, then the temporal and spatial spectra must be related as follows

$$F_{11}^1(k) = \frac{U_c}{2\pi} S_{11}\left(\frac{k_1 U_c}{2\pi}\right) \quad (7.18)$$

where

$$k_1 = 2\frac{\pi}{U_c} f. \quad (7.19)$$

Using the obtained definitions for the spatial and integral time scale in this equation it follows that

$$L_{11} = U_c I_t. \quad (7.20)$$

Single point similarity suggests, as this experiment has shown, that

- $L_{11} \propto x - x_0$
- $\overline{u^2} \propto (x - x_0)^{-2}$
- $U_c \propto (x - x_0)^{-1}$

so that equation the integral time scale I_t must go with the x-position squared.

$$I_t \propto (x - x_0)^2 \quad (7.21)$$

Plugging this result into equation 7.13

$$S_{11}(0) = 2\overline{u^2} I_t$$

suggests that power spectra should show no x-dependence for the very low frequency region.

7.5 Measured Spectra

Fig. 7.5 to 7.7 show the frequency spectra obtained at $x/D = 30.3, 43.3$ and 53.3 . The filter settings and the wire cut-off point

$$f_N \approx \frac{U_c}{2l_w} \quad (7.22)$$

are marked in each. The very highest frequencies are dominated by noise and harmonics, most likely associated with the CTA adjustments. These clearly are of very low values, and are irrelevant to the considerations here.

The different error bands are due to the fact that different numbers of blocks were averaged over for each data set. The relative error in the spectral amplitude is given by

$$\epsilon = \frac{1}{\sqrt{N}} \quad (7.23)$$

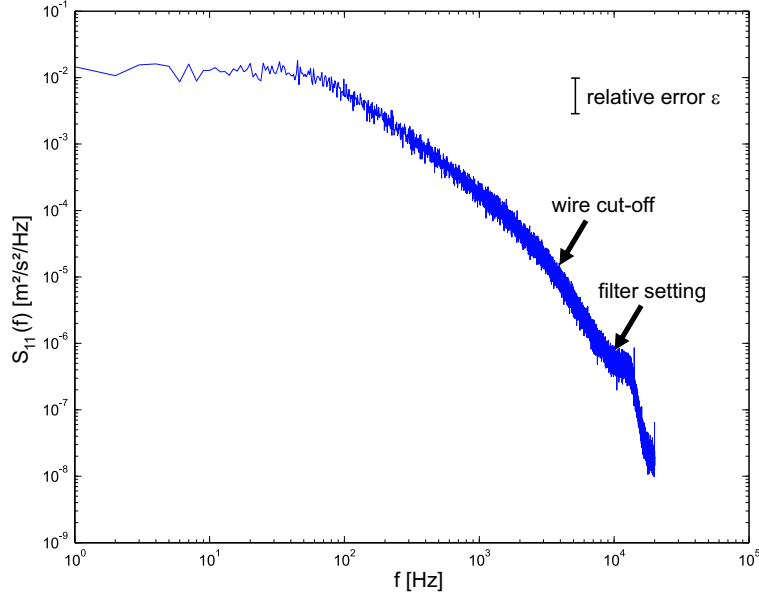


Figure 7.5: Power spectrum $S_{11}(f)$ at $x/D=30.3$ versus frequency f

where N is the number of blocks (George *et al.* [21]). The spectra were averaged over 30, 60 and 90 blocks yielding relative errors of 18.3%, 12.9% and 9.13%. In a log-log plot these errors show up as constants as presented in the figures.

The three power spectra are plotted together in fig. 7.8. The farther downstream a spectrum is measured, the less energy is found for high frequencies (as expected). At low frequencies however the spectral amplitude is nearly identical as suggested by similarity theory and FFH above.

The wavenumberspectra that were calculated based on Taylor's hypothesis are shown in fig. 7.9. Since the turbulence Reynolds number is constant with x in this flow, all scales are in constant ratios. Therefore, the scaled wavenumber spectra were also expected to collapse. The spectra were scaled as it is customary for homogeneous flows, the flow type the axial direction of the jet was found to adapt to in similarity variables.

$$\tilde{F}_{11}^1 = \frac{F_{11}^1}{U_c^2(x - x_0)} \quad (7.24)$$

$$\tilde{k}_1 = k_1 \cdot (x - x_0) \quad (7.25)$$

The three scaled wavenumberspectra \tilde{F}_{11}^1 can be seen in fig. 7.10. Indeed all those scaled spectra are identical for different downstream positions. The

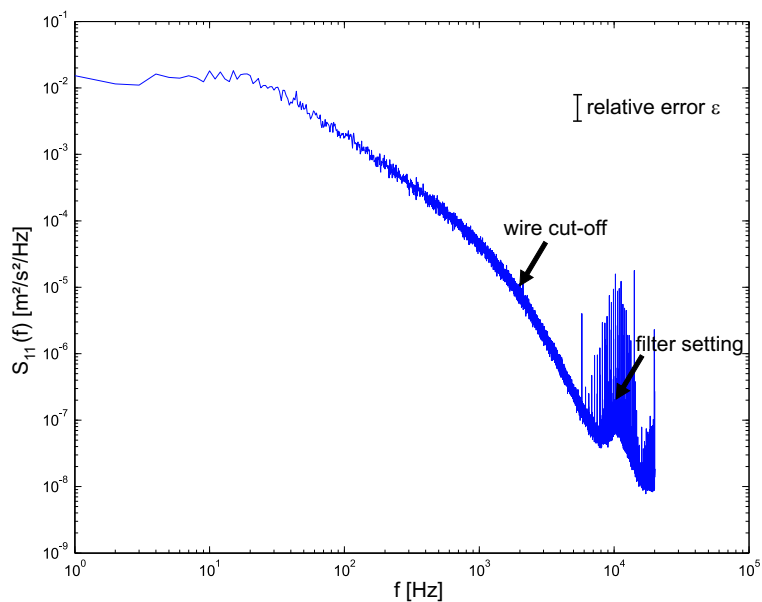


Figure 7.6: Power spectrum $S_{11}(f)$ at $x/D=43.3$ versus frequency f

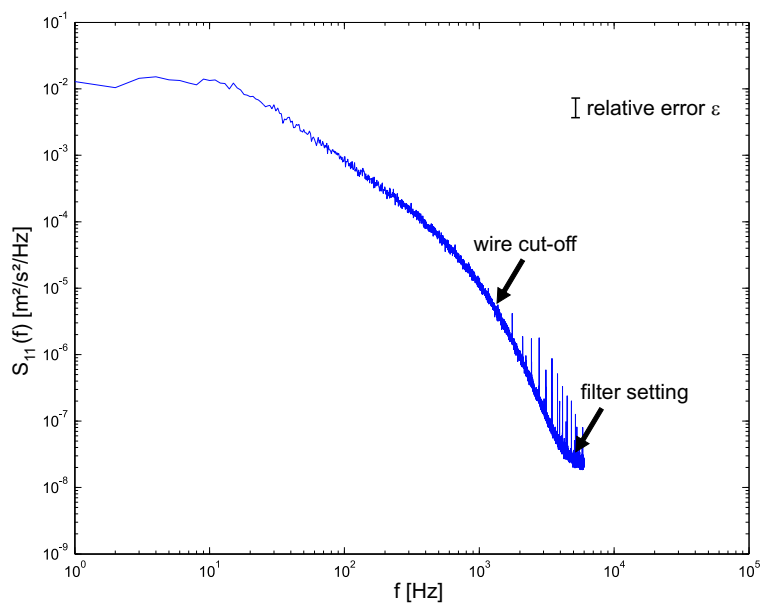


Figure 7.7: Power spectrum $S_{11}(f)$ at $x/D=58.3$ versus frequency f

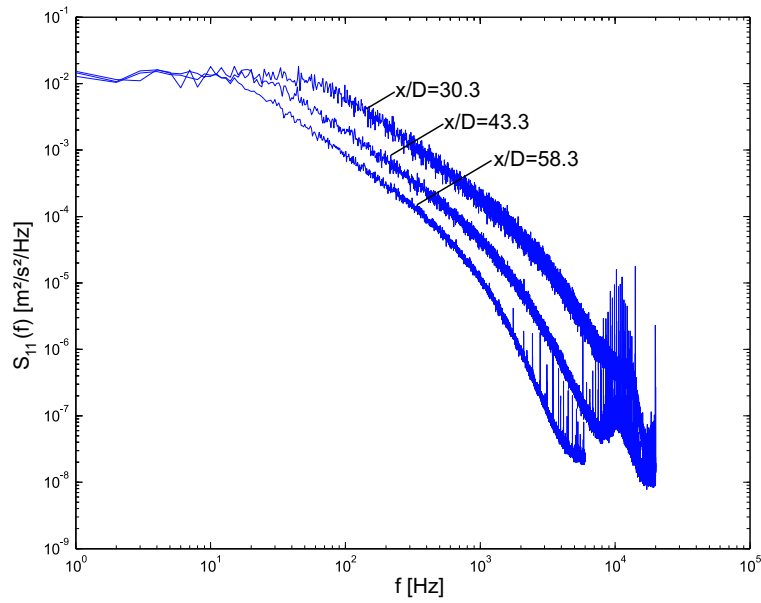


Figure 7.8: Comparison of the three power spectra. Note spectra at low frequencies are the same within uncertainty, consistent with similarity theory and applicability of Taylor's hypothesis

deviations that can be found for high wavenumbers are beyond the wire cut-off point and should therefore not be taken into consideration.

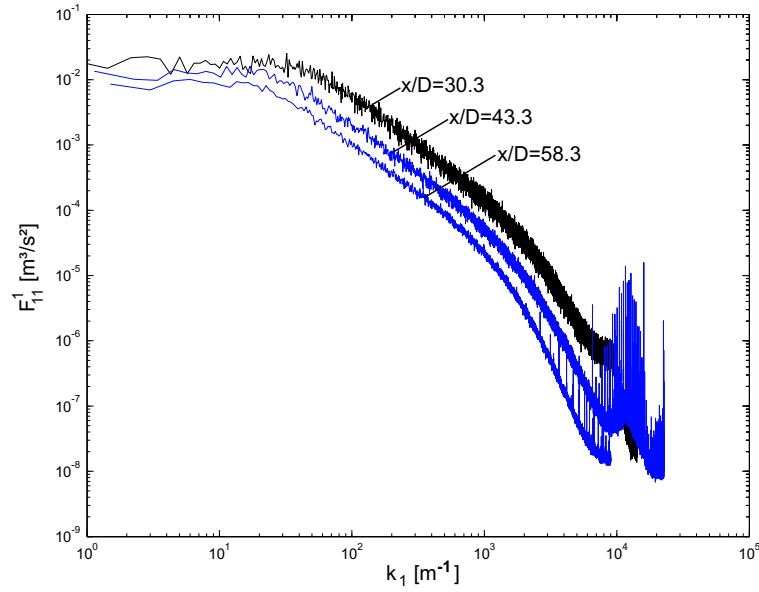


Figure 7.9: Wavenumber spectra $F_{11}^1(k_1)$ at $x/D=30.3$, 43.3 and 58.3 versus wavenumber k_1

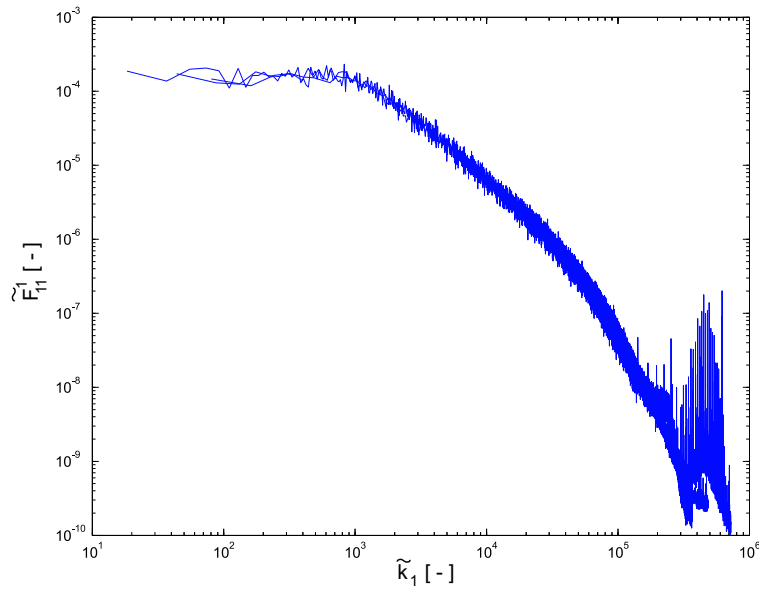


Figure 7.10: Scaled wavenumber spectra $\tilde{F}_{11}^1(\tilde{k}_1)$ at $x/D=30.3$, 43.3 and 58.3 versus scaled wavenumber \tilde{k}_1

Chapter 8

PIV Results and Future Work

This investigation of the streamwise two-point correlation of the axisymmetric turbulent jet provides evidence to support a theory concerned with the similarity analysis of the two-point velocity correlation tensor. In particular, the similarity analysis and its experimental confirmation imply that the double point velocity correlation tensor has a dependency on the similarity variables consistent with that of a homogeneous flow field in the streamwise direction. In this work, only measurements along the centerline of the jet were performed that confirm this behavior. Measurements at many radial positions were performed by Gamard [19, 20] but all at the same streamwise position. To test the theory's validity for the entire flow field, longitudinal correlation measurements off the centerline will be needed. Correlation curves obtained along lines of constant radial positions (in similarity variables, i.e. at a certain percentage of the halfwidth) should also collapse, since the flow field in similarity variables is homogeneous along those lines. With the current set up, measurements of this nature are not very satisfactory because the hot-wire introduces a significantly higher error with an increase in turbulence intensity.

Because of the positive result of the presented work, analysis of a data set of PIV (Particle Image Velocimetry) measurements from a water jet was initiated by co-workers Jakob Pedersen and Mohammed Elteyeb Eljack. This data was obtained by Fukushima, Aanen, and Westerweel at the Laboratory of Aero and Hydrodynamics at Delft Technical University, The Netherlands [18]. In principle it is possible to perform two-point correlation measurements using PIV. This technique permits multiple instantaneous measurements of the flow, so that the entire flow field can be captured at once. It unfortunately suffers from limitations which would have rendered it useless without the statistical certainty of the present work. Fig. 8.1 shows two-point correlations obtained from the PIV data. Scaling the separation in similar-

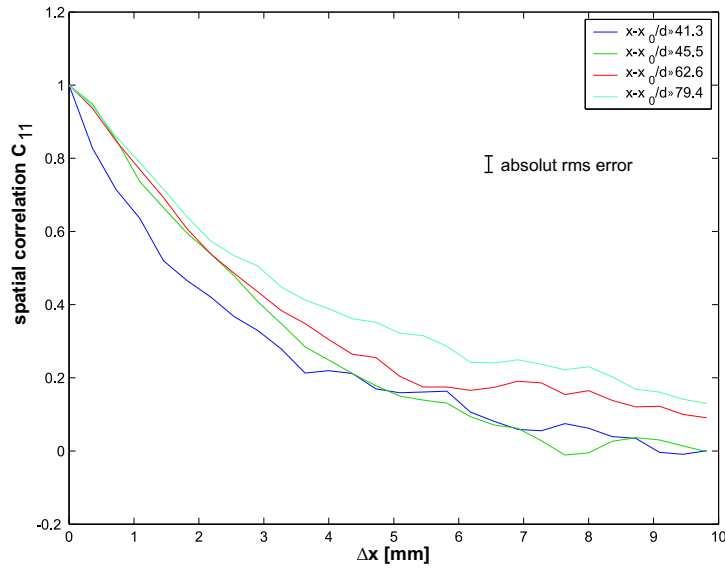


Figure 8.1: Spatial correlation of the axial velocity fluctuations obtained from PIV data

ity variables yields a collapse as shown in fig. 8.2. The deviations are considerably larger than from the data obtained from the combination of HW and LDA techniques because of the limited number of snapshots (600). They can be seen to collapse, however, within the statistical error which is 5 to 12 times larger than in the HW/LDA measurements. Since the PIV also captures the v -components of the fluctuations, the validity of the theory was tested for that case as well. The result is shown in fig. 8.3 and 8.4. The collapse in the latter can clearly be seen again.

The same data set will be analysed for off centerline correlations. To obtain those correlations with higher accuracies, the combination of two LDA systems might be considered. Measurements would surely become even more time consuming than with the combination of HW and LDA but might yield better results in the region of higher turbulence intensities.

The final goal is to implement this theory to the POD, yielding new possibilities of analyzing an unbounded inhomogeneous flow.

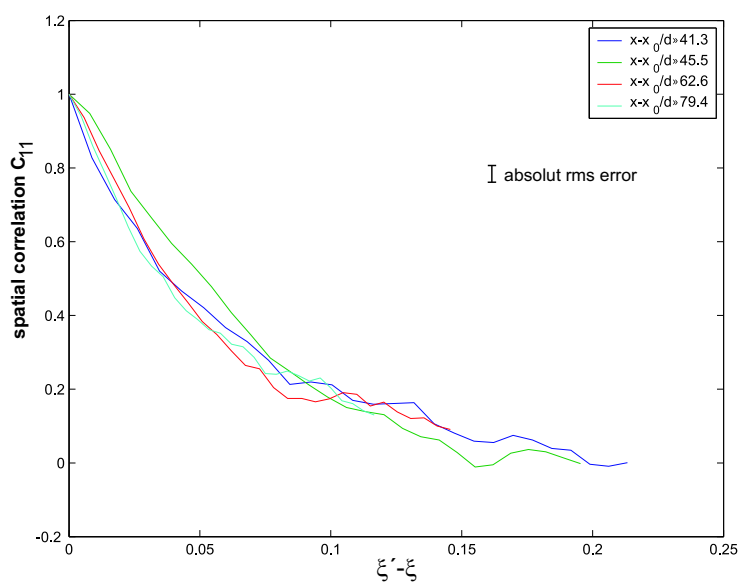


Figure 8.2: Spatial correlation of the axial velocity fluctuations in similarity coordinates

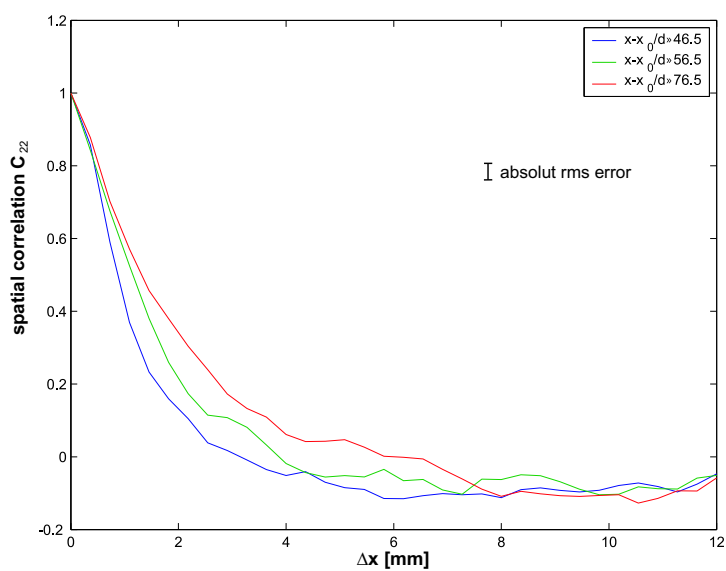


Figure 8.3: Spatial correlation of the radial velocity fluctuations obtained from PIV data

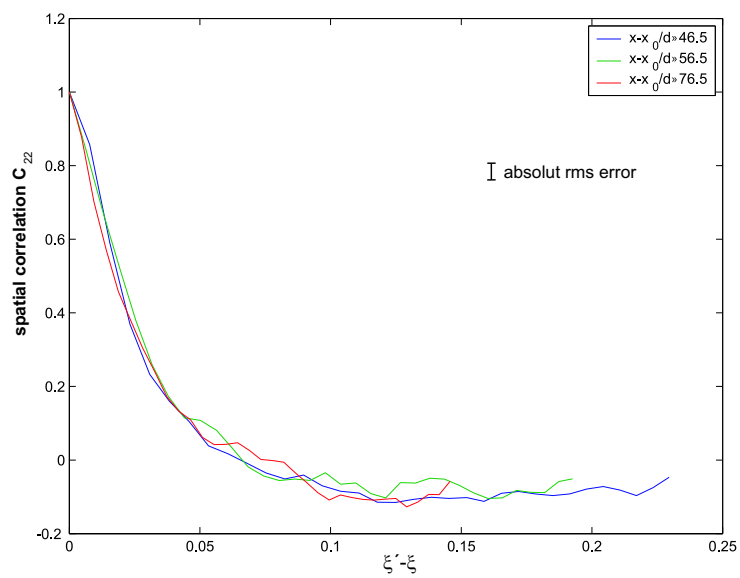


Figure 8.4: Spatial correlation of the radial velocity fluctuations in similarity coordinates

Chapter 9

Summary

A facility for the investigation of a free turbulent axisymmetric jet has been set up. The experimental set-up was enclosed in order to provide the possibility of uniform spatial seeding for optical measurement techniques. This enclosure was designed to be large enough to minimize the momentum loss due to backflow so that 99% of the momentum was retained until 80 diameters downstream. Thus, the jet could be considered to be only insignificantly influenced by the surrounding walls up to that position. In the far field of the axisymmetric free jet, i.e. in the region between 30 and 80 diameters downstream where the jet was shown to agree with *single point* similarity, spatial correlation measurements in longitudinal direction were performed.

The focus of the presented investigation was to obtain streamwise correlation measurements in the far jet to test the equilibrium similarity analysis of the *two-point* Reynolds stress equations. This theory implies a homogeneous flow field in similarity coordinates in axial and azimuthal direction of the axisymmetric turbulent far jet. In an earlier work this idea could be confirmed for a fixed downstream position. Due to a lack of experimental data however, the prediction of a homogeneous field in logarithmic coordinates for the streamwise direction could not be tested up to now.

In this work correlation measurements were obtained that filled the existing experimental gap. The selected measurement technique was a combination of CTA and LDA. This combination was chosen based on considerations concerning maximal accuracy and minimal measuring time. The two techniques were combined successfully so that simultaneous measurements at two different positions in the flow field could be obtained.

Correlations with separation in downstream direction were obtained starting at $x/D = 30.3, 43.3$ and 58.3 . The correlation curves were

rescaled in the predicted similarity variables and indeed collapsed indicating homogeneous behavior as proposed by equilibrium similarity. Due to the very high number of statistically independent samples the absolute rms-error was small and thus the collapse of the curves very distinct. Initiated by these positive results a PIV data set was investigated by coworkers. The collapse of the correlation of the axial fluctuations along the centerline was confirmed within the significantly higher error. Furthermore, the theory was applied to the v-component correlation also yielding collapsing curves in similarity coordinates.

The transformation of the streamwise direction of the jet into a homogeneous field opens new application possibilities for the POD: The solution of an unbounded, infinite flow becomes possible, and in fact the solution is known (Fourier modes in the transformed coordinates). The confirmed homogeneity in similarity coordinates might also be of great use in DNS and LES computations.

Taylor's frozen field hypothesis was applied to the autocorrelation curves obtained at the reference points for the spatial correlation measurements. Surprisingly, the transformed autocorrelations completely agreed with the measured spatial correlations and collapsed onto each other when scaled in similarity variables. This strong indication that Taylor's hypothesis can be applied to measurements along the jet centerline was confirmed by analysing the power spectra and their transformation into wavenumber spectra.

Bibliography

- [1] ADRIAN, R.J.; ORLOFF, K.L.: Laser anemometer signals: visibility characteristics and application to particle sizing. In: *Appl. Opt.*, **16**, 1977, pp. 677-684
- [2] ALBRECHT, H.: *Laser-Doppler Geschwindigkeitsmessungen*. Akademie Verlag Berlin, 1986
- [3] ARNDT, R.E.A.; GEORGE, W.K.: Investigation of the large-scale coherent structures in a jet and its relevance to jet noise. In: *Proc. of the Second Interagency Symposium on University Research in Transportation Noise*, North Carolina State University, Raleigh, NC, 1974
- [4] ARNDT, R.E.A.; LONG, D.F.; GLAUSER, M.N.: The Proper Orthogonal Decomposition of pressure fluctuations surrounding a turbulent jet. In: *Journal of Fluid Mechanics*, **340**, 1997, pp. 1-33
- [5] BAKER, C.B.: An analysis of the turbulent buoyant jet. PhD diss., Pennsylvania State University, University Park, PA, 1980
- [6] BAKER, C.B.; GEORGE, W.K.; TAULBEE, D.B.: An analysis of the axisymmetric turbulent buoyant jet. In: *Proc. of the 7th Int. Heat Transfer Conf.*, Munich, Germany, 1980
- [7] BEUTHER, P.D.; SHABBIR, A.; GEORGE, W.K.: X-wire response in turbulent flows with high intensity turbulence and low mean velocity. In: *Proc. ASME Symp. on Thermal Anemometry*, FED V53, Cincinnati, OH, 1987, pp. 39-42
- [8] BOERSMA, B.J.; BRETHOUWER, G.; NIEUWSTADT, F.T.M.: A numerical investigation on the effect of the inflow conditions on the self-similar region of a round jet. In: *Physics of Fluids*, **10**, 1998, pp. 899-909
- [9] BUCHAVE, P.; GEORGE, W.K.; LUMLEY, J.L.: The measurement of turbulence with the Laser-Doppler anemometer. In: *Ann. Rev. Fluid Mechanics*, **11**, 1979, pp. 443-503

- [10] CAPP, J.P.: Experimental Investigation of the Turbulent Axisymmetric Jet. PhD diss., Dept. Mech and Aero. Eng., SUNY/University at Buffalo, Buffalo, NY: 1983
- [11] CITRINITY, S.P.: Experimental Investigation into the Dynamics of the Axisymmetric Mixing Layer utilizing the Proper Orthogonal Decomposition. PhD diss., Dept. Mech and Aero. Eng., SUNY/University at Buffalo, Buffalo, NY: 1996
- [12] CITRINITI, J.H.; GEORGE, W.K.: Reconstruction of the global velocity field in the axisymmetric mixing layer utilizing the proper orthogonal decomposition. In: *Journal of Fluid Mechnaics*, **183**, 1994, pp. 67-73
- [13] DURST, F.; MELLING, A.; WHITELAW, J.H.: *Principles and practice of Laser-Doppler Anemometry*. London: Academic Press Inc., 1976
- [14] ERIKSSON, J.G.; KARLSSON, R.I.: An investigation of the spatial resolution requirements for two-point correlation measurements using LDV. In: *Experiments in Fluids*, **18**, 1994, pp. 393-396
- [15] EWING D.: On Multi-point Similarity Solutions in Turbulent Free Shear Flows. PhD diss., Dept. Mech. Eng., SUNY/University at Buffalo, Buffalo, NY, 1995
- [16] EWING, D.; GEORGE, W.K.: Application of a Similarity Hypothesis to the POD for Spatially Evolving Shear Layers. In: *Int. Symp. of Turbulent Heat and Mass Transfers*, Lisbon, Portugal, 1995, pp. 1.1.1-1.1.5.
- [17] EWING, D.; GEORGE, W.K.: Implication of a similarity hypothesis on the application of the proper orthogonal decomposition. In: *Proc. ICHMT Symposium on Turbulence, Heat and Mass Transfer (1994)*, Elsevier, Amsterdam, 1995
- [18] FUKUSHIMA, C.; AANEN, L.; WESTERWEEL, J.: Investigation of the Mixing Process in an Axisymmetric Turbulent Jet using PIV and LIF. In: *Proc. 10th Int. Symp. on Applications of Laser techniques to Fluid Mechanics* Lisbon, Portugal, 2000
- [19] GAMARD S.: The axisymmetric turbulent jet. PhD diss., Dept. Thermo and Fluid Dynamics, Chalmers University of Technology, Göteborg: 2002

- [20] GAMARD, S.: Application of the Slice POD to the Far Region of an Axisymmetric Jet. PhD diss., Dept. Mech and Aero. Engineering, SUNY/University at Buffalo, Buffalo, NY, 2002
- [21] GEORGE, W.K.; BEUTHER, P.D.; LUMLEY, J.L.: Processing of random signals. In: *Proceedings of the Dynamic Flow Conference*, Skovlunde, Denmark, 1978, pp. 757-800
- [22] GEORGE, W.K.: Insight into the dynamics of coherent structures from a proper orthogonal decomposition. In: *The Structure of near Wall Turbulence, Proc. of Symp. on Near Wall Turbulence*, Dubrovnik, Yugoslavia: Hemisphere, NY, 1988, pp. 168-180
- [23] GEORGE, W.K.: The self-preservation of turbulent flows and its relation to initial conditions and coherent structures. In: *Advances in Turbulence*, Hemisphere, NY, 1989, pp. 39-73
- [24] GEORGE, W.K.: Some thoughts on similarity, the POD, and finite boundaries. In: *Trends in Mathematics, Proc. of the Second Monte Verita Colloquium*, Birkhauser, Sw., 1999
- [25] GLAUSER, M.N.: Coherent Structures in the axisymmetric turbulent jet mixing layer. PhD diss., Dept. Mech and Aero. Eng., SUNY/University at Buffalo, Buffalo, NY, 1987
- [26] GLAUSER, M.N.; GEORGE W.K.: Orthogonal decomposition of the axisymmetric jet mixing layer including azimuthal dependence. In: *Advances in Turbulence*, Springer Verlag, 1987, pp. 357-366
- [27] GLAUSER, M.N.; TAYLOR, J.A.; UKEILEY, L.S. ET AL.: A low dimensional description of the axisymmetric turbulent jet: an update. In: *ERCRAFTAC Bulletin*, **46**, 2000, pp. 53-61
- [28] HJELMFELT, A.T.; MOCKROS, L.F.: Motion of discrete particles in a turbulent fluid. In: *Applied Scientific Research*, **16**, 1966, p. 149
- [29] HOLMES, P.; LUMLEY, J.L.; BERKOOZ, G.: *Turbulence, Coherent Structures, Dynamical Systems and Symmetry*. Cambridge, 1996
- [30] HUSSAIN, A.K.M.F.: Coherent structures - reality and myth. In: *Physics of Fluids*, **26** (10), 1983, pp. 2816-2850
- [31] HUSSEIN H.J.; CAPP, S.P.; GEORGE, W.K.: Velocity measurements in a high-Reynolds-number, momentum-conserving, axisymmetric, turbulent jet. In: *Journal of Fluid Mechanics*, **258**, 1994, pp. 31-75

- [32] JORDAN, P.; GERVAIS, Y.: Modelling self and shear noise mechanisms in anisotropic turbulence. In: *The 9th AIAA/CEAS Aeroacoustic Conference*, **AIAA 2003-8743**, Hilton Head, South Carolina, 2003
- [33] JUNG, D.: An Investigation of the Reynolds Number Dependence of the Axisymmetric Jet Mixing Layer using a 138 Hot Wire-Probe and the POD. PhD diss., Dept. Mech and Aero. Eng., SUNY/University at Buffalo, Buffalo, NY, 2001
- [34] JUNG, D.; GAMARD, S.; GEORGE, W.K. ET AL.: Downstream evolution of the most energetic POD modes in the mixing layer of a high Reynolds number axisymmetric jet. In: *Turbulent Mixing and Combustion, Proceedings of the IUTAM Symposium, Kingston 2001*, Kluwer Academic Publisher, Dordrecht, 2002, pp. 23-32
- [35] LUMLEY, J. L.: Interpretation of Time Spectra Measured in High Intensity Shear Flows. In: *Physics of Fluids*, **8**, 1965, pp. 1056-1062
- [36] LUMLEY, J.: The structure of inhomogeneous turbulent flows. In: *Atmospheric Turbulence and Radio Wave Propagation*, (ed. A.M. Yaglom and V.I. Tatarsky), Moscow, USSR, 1967
- [37] MONIN, A.S.; YAGLOM, A.M.: *Statistical Fluid Mechanics, Mechanics of Turbulence*. MIT Press, Cambridge, MA, 1971
- [38] PANCHAPAKESAN, N.R.; LUMLEY, J.L.: Turbulence measurements in axisymmetric jets of air and helium, part 2 helium jets. In: *Journal of Fluid Mechanics*, **246**, 1993, pp. 225-247
- [39] REYNOLDS, O.: An experimental investigation of the circumstances which determine whether the motion of water shall be direct or sinuous, and of the law of resistance in parallel channels. In: *Phil. Trans. Roy. Soc.*, **174**, 1883, pp. 935-982
- [40] TAYLOR, G.I.: The spectrum of turbulence. In: *Proceedings of the Royal Society of London*, **A164**, 1938, pp. 476-490
- [41] TENNEKES, H.; LUMLEY, J.L.: *A first course in turbulence*. MIT Press, Cambridge, MA, 1972
- [42] TUTU, N.; CHEVRAY, R.: Cross-wire anemometry in high intensity turbulence. In: *Journal of Fluid Mechanics*, **71**, 1975, pp. 785-800
- [43] TOLLMIEHN, W.: Berechnung turbulenter Ausbreitungsvorgänge. In: *Zur Angewandten Mathematik und Mechanik*, **6**, 1926, pp. 468-478

- [44] WYGNANSKY, I.; FIEDLER, H.: Some measurements in the self-preserving jet. In: *Journal of Fluid Mechanics*, **38**, 1969, pp. 577-612